Terahertz Laser Radiation Induced Resistivity Oscillations in GaAs Heterostructures

Dissertation

zur Erlangung des Doktorgrades
der Naturwissenschaften (Dr. rer. nat.)
der Fakultät für Physik
der Universität Regensburg

vorgelegt von

Tobias Herrmann

aus Dresden

im Jahr 2019

Promotionsgesuch eingereicht am: 09.10.2018

Die Arbeit wurde angeleitet von: Prof. Dr. Sergey D. Ganichev

Prüfungsauschuss

Vorsitzender: Prof. Dr. Vladimir Braun

1. Gutachter: Prof. Dr. Sergey D. Ganichev

2. Gutachter: Prof. Dr. Christian Schüller

weiterer Prüfer: Prof. Dr. Josef Zweck

Contents

1 Introduction

The research on two dimensional electron gases (2DEG) has been playing a central role in solid state physics in the last fifty years, yielding major progress in semiconductor technology [1, 2] and fundamental research [3]. The Nobel Prize awarded integer [4] and fractional quantum Hall effect [5–7] are the most prominent examples of phenomena observed in such systems, both in a regime of strong magnetic fields, where a strong quantization has to be considered.

Not only in this regime fascinating effects occur. Also in the range of lower magnetic fields where classical or semi-classical approaches can be used. Two examples of such effects are the commensurability modifications of the resistance induced by periodic potentials, known as Weiss-oscillations [8, 9], and the magnetoresistance oscillations generated by external fields applied additionally to the magnetic field [10]. To the latter count, e.g. the Hall field induced resistance oscillations [11], the phonon induced resistance oscillations [12, 13], and the microwave induced resistivity oscillations (MIRO) [14]. Especially the observation of zero resistance states (ZRS) in the context of MIRO [15, 16] has drawn a lot of attention. Many experimental works on MIRO have been reported over the last eighteen years [15–37]. Although several models have been developed [38–42], there is still no commonly accepted theoretical explanation of the phenomenon [43, 44]. In particular three open questions remain: Firstly, whether they are a phenomenon which occurs on the boundaries of a 2DEG and the respective contacts [45] or environment, which can be, e.g. air or vacuum [38], or whether it occurs in the whole 2DEG [42, 46]. Secondly, it has to be clarified how strongly the oscillations are influenced by the polarization of the applied radiation [23]. And as a third open question, the behavior of MIRO when illuminated with high intensity radiation was studied lately [29, 35] in the microwave range, but high intensity data induced by higher frequencies are yet to be obtained. Such data would demonstrate the robustness of the effect, even under extreme experimental conditions on the one hand and would help to understand the underlying mechanisms on the other.

This thesis is devoted to the study of radiation induced resistivity oscillations in GaAs 2DEG, not induced by microwaves but by terahertz (THz) radiation.

Although most works on MIRO are performed in the microwave range, it was shown that MIRO-like oscillations can also be induced by high frequency radiation [32, 36, 37]. Here, the advantages of THz laser radiation, which are not present in the microwave range, are exploited to provide answers to the open questions in the field of MIRO. The study shows, that, indeed, the observed THz induced photoconductivity oscillations are MIRO. In this thesis also the question, whether the observed oscillations originate from the sample boundaries, or whether the effect stems from the whole 2DEG, is answered. This allows to determine which of the theories addressed above can be employed on the observed oscillations. In the following the results are analyzed in the framework of those theories. Furthermore, the helicity dependence of MIRO is intensely studied. The analysis shows that the influence of the radiations helicity is weaker than theoretically expected. Consequently, possible reasons for this discrepancy are discussed. Furthermore the study reports on the irradiation of GaAs 2DEG with high power radiation. There, MIRO are observed for several frequencies and in a intensity range of five orders of magnitude. Based on these observations the corresponding saturation mechanisms are discussed.

In detail, this thesis is structured as follows: Chapter 2 is devoted to the physical background of MIRO and an overview over preliminary works on the topic. It starts with a general description of a 2DEG in Sec. 2.1.1 and with the mechanisms describing magnetotransport in such a system in Sec. 2.1.2. Afterwards radiation related phenomena in a 2DEG are discussed, including cyclotron resonance (CR) in Sec. 2.2.1 and electron gas heating in Sec. 2.2.2. Finally, in Sec. 2.2.3, MIRO are discussed on the basis of preliminary works on this effect and the displacement and the inelastic mechanism are introduced in Sec. 2.2.4. The second chapter gives an overview over the applied methods. It starts with the description of the probed samples in therms of material properties and the used contact geometries in Secs. 3.1.1 and 3.1.2, respectively. Afterwards the radiation sources and the different experimental setups used in this work are described in Sec. 3.2. In chapter 4 the experimental results are presented and discussed. The first part, Sec. 4.1.1 is devoted to the presentation of the photoconductivity data featuring THz induced magneto-oscillations Then, it is demonstrated that the observed oscillations feature exactly the same properties as MIRO in Sec. 4.1.2, which in turn allows to treat

them as the same effect. In the following section, 4.2.1, the oscillations are studied by selective illumination of either only the bulk or the boundaries. The results show, that MIRO is a bulk effect, which in turn allows on to conclude which theory describes the observed oscillations best. Consequently the data is analyzed in therms of the respective mechanisms in Sec. 4.2.2. Afterwards the helicity dependence of MIRO is studied in Sec. 4.3.1 and the results for different polarizations are discussed in Sec. 4.3.2. In Sec. 4.4 photoconductivity oscillations induced by high intensity THz radiation are presented. They show a strong saturation for high intensities. The underlying saturation mechanisms are discussed in Sec. 4.4.2. Finally, chapter 5 summarizes the work and gives an outlook to further research on MIRO.

2 Physical Background and Preliminary Works

This chapter's purpose is to introduce the fundamental principles necessary to get an understanding of this work. Therefore a short introduction to the dimensional electron gases (2DEG), the systems in which MIRO are observed is given. Afterwards the carrier transport and radiation absorption in a 2DEG will be discussed. The last part of this chapter is devoted to give an overview of both experimental and theoretical preliminary work on MIRO.

2.1 Two-Dimensional Electron Gas

Two dimensional electron gases play a crucial role when it comes to designing high mobility semiconductor structures, which are of tremendous importance in modern electronic technology [1, 2]. Their role in solid state physics, however, is not less important. The quantum Hall effect [4] is, for instance, a fundamental effect discovered in a 2DEG. The following example for the band engineering of a 2DEG is adapted from Ref. [47].

2.1.1 Band Structure of the Two-Dimensional Electron Gas

A 2DEG can be realized when two semiconductor materials with different band gaps but similar lattice constants are stacked on top of each other. Figure 1 (a) shows the band structures of two such semiconductors, A and B, before assembly. Following Anderson's rule the vacuum levels of the two materials line up [47]. The vacuum level alignment leads to potential differences $\Delta\varepsilon_\mathrm{c}$ and $\Delta\varepsilon_\mathrm{v}$ for both, the conduction and the valence band. When the two materials are assembled and if they are doped, for example one p- and one n-typed, a charge transfer takes place. This leads to the formation of a dipole layer and, correspondingly, to that to a band bending at the heterojunction. Figure 1 (b) shows this for the two exemplary materials. Here, the one with the large band gap ε_g^A is n-doped, whereas the one with the smaller gap E_g^B is slightly p-doped. When thermal equilibrium is achieved the Fermi levels are matched up in the region of the junction. If the new Fermi level is now higher than the minimum of the bended conduction band, electrons are trapped in a potential well being

roughly triangular. $\Delta\varepsilon_c$ prevents electrons and holes from recombining and the electrostatic potential in between squeezes the electrons towards the interface. The potential well is usually about 10 nm thick, and the electron movement is restricted in growth direction of the semiconductor structure. The growth direction is defined as z in this work. In the orthogonal directions x and y, however, the electrons can move freely. This is the two-dimensional electron gas. This method of growth with the donors lying at a distance from the 2DEG is referred to as modulation doping and yields two main benefits: besides the confinement of electrons to two directions addressed above, the donors and electrons are separated, and therefore scattering by ionized impurities is reduced and high mobilities can be achieved.

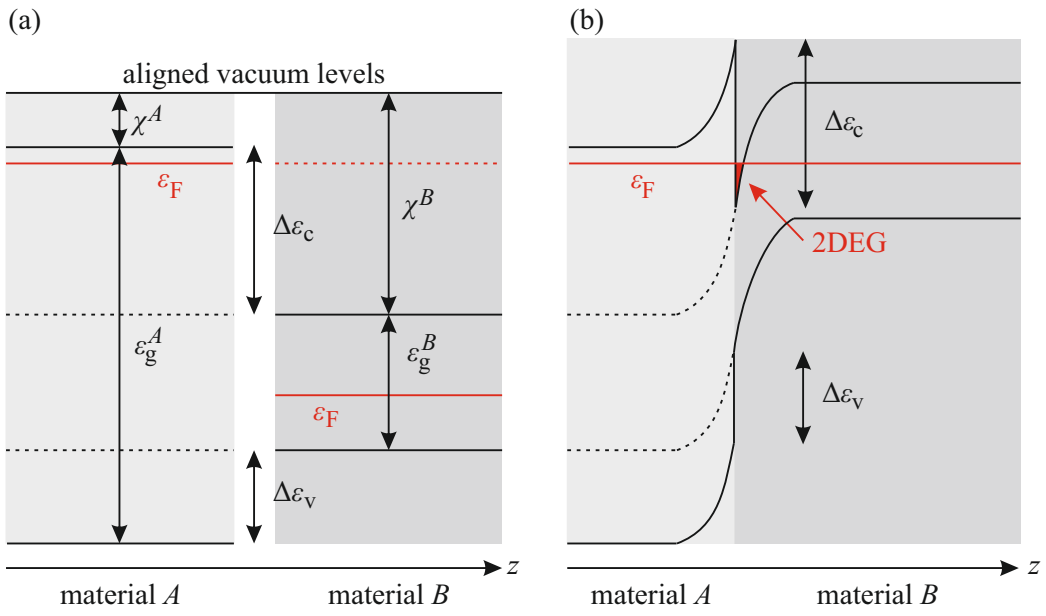

Figure 1: Conduction and valence bands of two semiconductors, A and B, before (a) and after (b) thermal equilibration. The material growth direction is represented by z. Vacuum levels are aligned, shown in panel (a) following Anderson's rule. (b) Fermi levels are aligned yielding a band bending, leading to a roughly triangular potential well. Adapted from [47].

The restriction in z yields an energy quantization of the electrons in the 2DEG which is discussed in the following. To calculate the electron wave functions and their energy eigenvalues the 2DEG potential will be approximated as a perfect

triangular potential well. For simplification the potential barrier at $z < 0$ is defined as finitely high. For $z > 0$ a linear potential $V(z) = eEz$ is assumed. It describes an electron of the charge e in an electric field E. The free carrier motion in the 2DEG plane is not related to the confinement in z-direction. Hence a product approach to the wave function can be taken, which reads as

$$\psi(\boldsymbol{r}) = e^{ik_x x} e^{ik_y y} \phi(z). \tag{1}$$

With $\phi(z)$ being the z-dependent part of the wave equation, one can write the one dimensional Schrödinger's equation [47]

$$\left[-\frac{\hbar^2}{2m_z^*} \frac{d^2}{dz^2} + eEz \right] \phi(z) = \varepsilon \phi(z). \tag{2}$$

In order to solve it the dimensionless quantities $\bar{z} = z/z_0$ and $\bar{\varepsilon} = \varepsilon/\varepsilon_0$ are defined, where

$$z_0 = \left(\frac{\hbar^2}{2meE} \right)^{1/3}, \quad \varepsilon_0 = \left[\frac{(eE\hbar)^2}{2m} \right]^{1/3} = eEz_0. \tag{3}$$

Schrödinger's equation reduces now to the Airy equation [47]

$$\frac{d^2\phi}{ds^2} = s\phi, \tag{4}$$

with the new independent variable $s = \bar{z} - \bar{\varepsilon}$. The Airy equation has two independent solutions $\mathrm{Ai}(s)$ and $\mathrm{Bi}(s)$ [47]. Two requirements have to be fulfilled in order to obtain an applicable solution: The boundary condition at $z = 0$ requires $\phi(z = 0) = \phi(s = -\varepsilon_0) = 0$. Both Airy functions oscillate for negative (s), and consequently the energies of the bound states of the triangular well are found for the functions being zero. Moreover the wave function should be well defined for $z \to +\infty$. Therefore, the solution $\mathrm{Bi}(s)$ can be neglected, since it diverges for $s \to +\infty$ [48]. For $\mathrm{Ai}(s)$ however there is an infinite number

n of negative s-values where it equals zero, which are called $-c_n$ here. To make sure that $\phi(z = 0) = 0$ is fulfilled, $\bar{\varepsilon} = c_n$ is necessary and the allowed energies are given by

$$\varepsilon_{n,z} = c_n \left[\frac{(eE\hbar)^2}{2m_z^*} \right]^{1/3}, \quad \text{with } n = 1, 2, 3, \dots , \tag{5}$$

and m_z^* being the effective electron mass in z-direction.

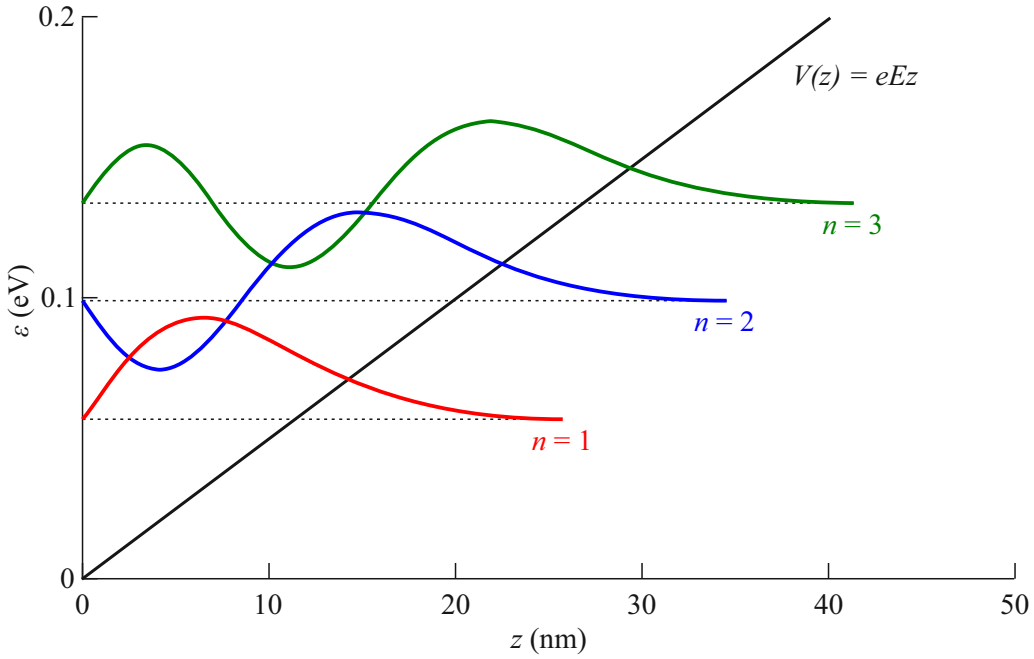

Figure 2: Energy levels (dashed lines) and corresponding wave functions (colored solid lines) of a triangular potential well with potential energy $V(z)$. The scales are for electrons in GaAs and an electric field $E = 5\,\mathrm{MV\,m^{-1}}$. Adapted from [47].

The respective unnormalized one dimensional wave functions are

$$\phi_n(z) = \mathrm{Ai}(s) = \mathrm{Ai}\left(\frac{eEz - \varepsilon}{\varepsilon_0} \right). \tag{6}$$

Following the product approach in Eq. (1), the three dimensional energy eigenvalues are given by

$$\varepsilon_i(k_x, k_y) = \varepsilon_{n,z} + \frac{\hbar^2 k_x^2}{2m_x^*} + \frac{\hbar^2 k_y^2}{2m_y^*} \ , \tag{7}$$

containing the effective electron masses m_x^*, m_y^*, and the electron wave vectors k_x and k_y [47].

2.1.2 Electron Transport in Two Dimensions

This work is devoted to study the influence of external experimental parameters like magnetic fields and terahertz radiation on the electron motion in a 2DEG. The microscopic description in this section will mainly follow the logic of Ref. [49]. When it comes to electron motion Ohm's law

$$\boldsymbol{j}(\boldsymbol{r}) = \sigma \boldsymbol{E}(\boldsymbol{r}) \tag{8}$$

is best to start with. It states that the electric current density $\boldsymbol{j}(\boldsymbol{r})$ and the electric field $\boldsymbol{E}(\boldsymbol{r})$ driving the electrons, are proportional to each other. The constant linking them together is the electrical conductivity σ, which is independent on the direction $\boldsymbol{r}$ in a homogeneous conductor.

Though, the electrical conductivity depends on the conducting material, the material shape determines whether the electrons can move in three or just two dimensions. From a microscopic perspective, the material dependence of the conductivity is described by the Drude model and based on the scattering probability of an electron in the respective material. Scattering is possible, i. a. with crystal defects, or phonons.

In this work two fields are applied: An electric field in the 2DEG plane, for instance $\boldsymbol{E} = (E, 0, 0)$, and a magnetic field $\boldsymbol{B} = (0, 0, B)$ perpendicular to it. The electrons are then accelerated by the Lorentz force $\boldsymbol{F} = -e\boldsymbol{E} - e\boldsymbol{v} \times \boldsymbol{B}$ and the motion between two scattering events can be described by Newton's equations

$$\frac{dv_x}{dt} = -\frac{|e|}{m^*}(E + v_y B),$$

$$\frac{dv_y}{dt} = +\frac{|e|}{m^*} v_x B. \tag{9}$$

These equations can be rewritten as

$$\frac{dv_x}{dt} = -\omega_c (v_D + v_y),$$

$$\frac{dv_y}{dt} = +\omega_c v_x. \tag{10}$$

introducing the cyclotron frequency $\omega_c = |e|B_z/m^*$ and the drift velocity $v_D = E/B$. The solution of Eq. (10) is

$$\mathbf{v}(t) = \begin{pmatrix} 0 \\ -v_D \end{pmatrix} + \begin{pmatrix} v_y(0) + v_D \\ -v_x(0) \end{pmatrix} \sin(\omega_c t) + \begin{pmatrix} v_x(0) \\ v_y(0) + v_D \end{pmatrix} \cos(\omega_c t). \tag{11}$$

Here $t = 0$ represents the time when the last scattering event took place leaving the electron with the velocity $(v_x(0), v_y(0)$. The first term on the right hand side describes the drift motion, which is normal to the magnetic and the electric field direction. The second and third term represent a circular motion with the frequency ω_c, called cyclotron motion. The electron transport is strongly influenced by the cyclotron motion, being controlled by the product of cyclotron frequency and the average scattering time τ_q. In the case of small magnetic fields, i.e. $\omega_c \tau_q \ll 1$, the electrons can not complete a full cyclotron orbit without being scattered. The case $\omega_c \tau_q \gg 1$, in which one or even multiple cyclotron orbits are completed yields some drastic differences compared to the first case, as will be discussed later in this section.

On large time scales $t \gg \tau_q$ the electron will perform a drift motion. Under the assumption that an electron has as drift velocity v_0 in a random direction after a collision which is independent of the direction before the scattering the drift velocity can be calculated. Following this assumption the probability $\mathcal{P}(\varphi)d\varphi$ that the electron moves into direction φ after the collision is expressed by

$$\mathcal{P}(\varphi)d\varphi = d\varphi/2\pi. \tag{12}$$

Additionally to the direction the time until the next scattering event has to be considered. The rate equation $dP(t)/dt = -wP(t)$, which correlates the probability $P(t)$ that an electron has not been scattered until the time t and the probability wdt that an electron is scattered within an infinitesimal time interval dt, has the solution $P(t) = Ce^{-wt}$. Here $C = 1$ can be derived from the initial condition $P(0) = 1$. The probability that the electron scatters within the time interval $[t, t + dt]$ is given by the product $p(t) = P(t)w(t)$. The mean scattering time is now

$$\tau_q = \int_0^\infty dtwe^{-wt}t = \frac{1}{w},$$

and

$$p(t)dt = e^{-t/\tau_q}\frac{dt}{\tau_q}. \tag{13}$$

From Eq. 10 one obtains the drift velocity by multiplying $\mathbf{v}$ with the probabilities $\mathcal{P}(\varphi)d\varphi$ and $p(t)dt$ and integrating over t and φ, which reads as

$$\bar{v} = \int_0^{2\pi} d\varphi\mathcal{P}(\varphi)\int_0^\infty dtp(t)\mathbf{v}(t). \tag{14}$$

Consequently, the components of the drift velocity are given by

$$\bar{v}_x = -v_D\frac{\omega_c\tau_q}{1+\omega_c^2\tau_q^2} = -E_x\frac{|e|\tau_q/m^*}{1+\omega_c^2\tau_q^2},$$

$$\bar{v}_y = -v_D\frac{\omega_c^2\tau_q^2}{1+\omega_c^2\tau_q^2} = -v_D\left(1-\frac{1}{1+\omega_c^2\tau_q^2}\right). \tag{15}$$

Note that for zero magnetic field strength B the mean drift velocity vanishes in y-direction, and reduces to a zero magnetic field value induced by the applied electric field in direction of x. The proportionality constant connecting the electric field and the drift velocity $\bar{v}_x$ at $B = 0$ is the mobility, given by

$$\mu = \frac{|e|\tau_p}{m^*}, \tag{16}$$

with the transport lifetime, given by

$$\tau_p^{-1} = \int_0^{2\pi} d\varphi(1 - \cos(\varphi))\mathcal{P}(\varphi). \tag{17}$$

From equation (15) one immediately sees the properties of the Hall effect: Under orthogonal application of an electric field and a magnetic field, the direction of the average electron drift deviates from the electric field direction by the Hall angle θ, obeying

$$\tan\theta = \frac{\bar{v}_y}{\bar{v}_x} = \omega_c\tau_p = \mu B. \tag{18}$$

The current density is given by

$$j_x = -n_\mathrm{s}|e|\bar{v}_x = \frac{n_\mathrm{s}e^2\tau_p}{m^*}\frac{1}{1+\omega_c^2\tau_p^2}E_x,$$

$$j_y = -n_\mathrm{s}|e|\bar{v}_y = \frac{n_\mathrm{s}e^2\tau_p}{m^*}\frac{\omega_c\tau_p}{1+\omega_c^2\tau_p^2}E_x. \tag{19}$$

Applying this result to Ohm's law, see Eq. (8), one asserts that at finite magnetic field normal to the 2DEG plane, the conductivity is a second rank tensor with the components

$$\sigma_{xx} = \frac{n_\mathrm{s} e^2 \tau_p}{m^*} \frac{1}{1 + \omega_c^2 \tau_p^2}$$

$$\sigma_{xy} = \frac{n_\mathrm{s} e^2 \tau_p}{m^*} \frac{\omega_c \tau_p}{1 + \omega_c^2 \tau_p^2}. \tag{20}$$

The missing tensor components can be taken from the same calculation as above but for an electric field in y-direction. This gives $\sigma_{yy} = \sigma_{xx}$ and $\sigma_{yx} = -\sigma_{xy}$. Ohm's law can now be written as

$$\begin{pmatrix} j_x \\ j_y \end{pmatrix} = \begin{pmatrix} \sigma_{xx} & \sigma_{xy} \\ -\sigma_{xy} & \sigma_{xx} \end{pmatrix} \begin{pmatrix} E_x \\ E_y \end{pmatrix}. \tag{21}$$

Note that Ohm's law can also be written in terms of resistivity

$$\begin{pmatrix} E_x \\ E_y \end{pmatrix} = \begin{pmatrix} \rho_{xx} & \rho_{xy} \\ -\rho_{xy} & \rho_{xx} \end{pmatrix} \begin{pmatrix} j_x \\ j_y \end{pmatrix}. \tag{22}$$

with the resistivity tensor ρ being the inverted conductivity tensor

$$\begin{pmatrix} \rho_{xx} & \rho_{xy} \\ -\rho_{xy} & \rho_{xx} \end{pmatrix} = \begin{pmatrix} \sigma_{xx} & \sigma_{xy} \\ -\sigma_{xy} & \sigma_{xx} \end{pmatrix}^{-1} = \frac{1}{\sigma_{xx}^2 + \sigma_{xy}^2} \begin{pmatrix} \sigma_{xx} & -\sigma_{xy} \\ \sigma_{xy} & \sigma_{xx} \end{pmatrix}. \tag{23}$$

With rising magnetic fields additionally quantization effects have to be taken into account and $\mu B = \omega_c \tau_p \gg 1$. This means that electrons complete multiple cyclotron orbits. Since the electron has also a wave character, it can interfere with itself. This interference is constructive for a certain phase and, therefore, it splits the former constant density of states n_{DOS} of the 2DEG into discrete energy levels ε_l, called Landau levels.

In order to get the values of the Landau levels, Schrödinger's equation for the potential $V(z)$ under influence of an external magnetic field

$$\left[\frac{1}{2m^*}(\boldsymbol{p}+e\boldsymbol{A})^2+V(z)\right]\psi=\varepsilon\psi \tag{24}$$

has to be solved. For a magnetic field $\boldsymbol{B}=(0,0,B)$ normal to the 2DEG plane one obtains the vector potential $\boldsymbol{A}=(A_x,A_y,0)$. Similar to the procedure in Sec. 2.1, a product approach

$$\psi(x,y,z)=\theta(x,y)\phi(z) \tag{25}$$

is chosen where the in- and out-of-plane Hamiltonians get separated, yielding the equations

$$\frac{1}{2m^*}\left[(p_x+eA_x)^2+(p_y+eA_y)^2\right]\theta(x,y)=\varepsilon_{xy}\,\theta(x,y) \tag{26}$$

and

$$\left[\frac{1}{2m^*}p_z^2+V(z)\right]\phi(z)=\varepsilon_z\phi(z) \tag{27}$$

with $\varepsilon=\varepsilon_{xy}+\varepsilon_z$.

Equation (27) is identical to Eq. (2), the one dimensional Schrödinger's equation from Sec. (2.1), with the subband energies ε_i from Eq. (5) representing the eigenvalues ε_z. For simplicity the vector potential $\mathrm{A}=(-yB,0,0)$, known as the Landau gauge, is chosen and inserted to Eq. (26). This gives

$$\frac{1}{2m^*}\left[p_y^2+(p_x-eBy)^2\right]\theta(x,y)=\varepsilon_{xy}\theta(x,y). \tag{28}$$

To solve this equation, again a separation approach

$$\theta(x,y)=e^{ik_x x}\eta(y) \tag{29}$$

is used. Together with $\omega_c = |e|B/m^*$ and $p_x = -i\hbar(\partial/\partial x)e^{ik_x x} = \hbar k_x$, Schrödinger's equation now reads

$$\left[\frac{p_y^2}{2m^*} + \frac{m^*}{2}\omega_c^2\left(\frac{\hbar k_x}{eB} - y\right)^2\right]\eta_{k_x}(y) = \varepsilon\eta_{k_x}(y), \tag{30}$$

which is the equation for a one-dimensional harmonic oscillator with the potential minimum shifted by the value $y_0 = \frac{\hbar k_x}{eB}$. For this equation the eigenstates are

$$\varepsilon_l = \hbar\omega_c(l + 1/2), \quad l = 0, 1, 2, \ldots \tag{31}$$

The quantized energy is independent of k_x, hence all states with different k_x but the same l are degenerate. These degenerate states together form a Landau level. The density of states $n_{\mathrm{DOS}}(\varepsilon)$, which is continuous for free electrons and represented by the gray box in Fig. 3 (a), is replaced by a sequence of δ-functions at the Landau levels, represented by the blue lines. The total energy of the system consists of the three different contributions

$$\varepsilon_{i,l,s} = \varepsilon_{z,n} + \varepsilon_{xy,l} + sg^*\mu_B B. \tag{32}$$

In this equation $\varepsilon_{z,i}$ describes the energy subbands due to the confinement in z-direction and $\varepsilon_{xy,l}$ the Landau levels. The additional term describes the energy difference due to spin splitting with $s = \pm 1/2$ being the spin quantum number, g^* being the effective Landé-factor, and μ_B being Bohr's magneton. Since spin does not play a role in this work, the last term will be neglected in the following considerations.

Since the cyclotron frequency ω_c depends linearly on B, so does the Landau level separation, see Fig. 3 (b). They are highly degenerate and carry the number

$$n_l = n_{DOS}(E)\hbar\omega_c = \frac{g_s eB}{h} \tag{33}$$

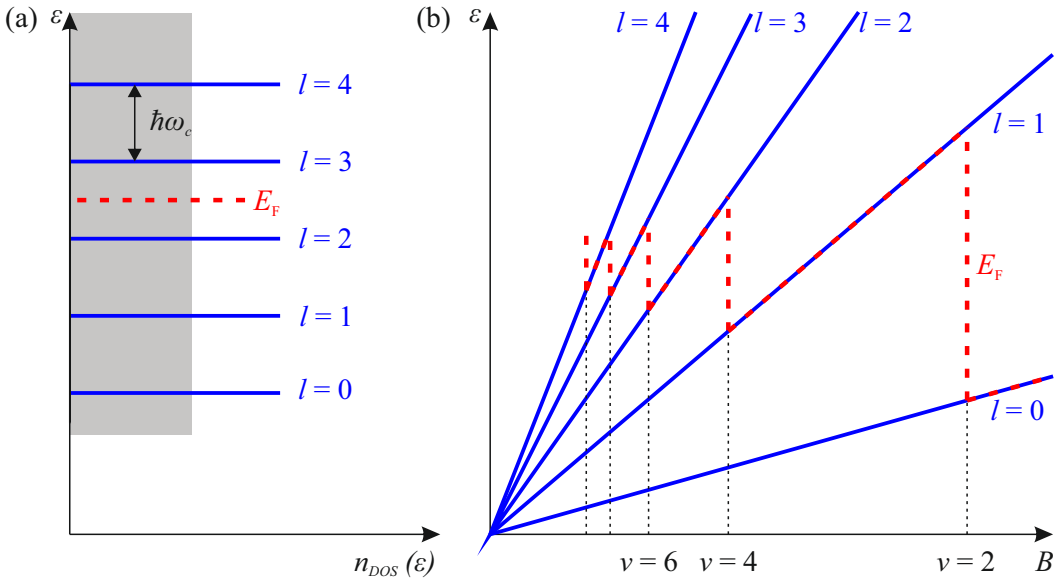

Figure 3: Energy of the first Landau levels for the lowest subband ($n = 1$) as a function of (a) the density of states n_{DOS} and (b) the magnetic field B. Panel (a) shows that the energy levels, represented by the blue lines, are equidistant, separated by the factor $\hbar\omega_c$. The electron distribution for free electrons is sketched by the gray box. In panel (b) the Fermi energy oscillates as function of the filling factor ν for fixed carrier density n_e. Adapted from refs. [47, 49].

of states per unit area and per spin orientation. If the s pin degeneracy is not lifted the Landé factor g_s equals two. The filling factor

$$\nu = 2n_e/n_l = hn_e/eB \tag{34}$$

compares the number of total electrons n_e in the system to the number of states per Landau level n_l. In experiment, with increasing magnetic field, $\hbar\omega_c$ and consequently n_l also increase. Since n_e is constant, the number of occupied Landau levels decreases for rising magnetic fields and the Fermi energy drops to deeper Landau levels at even filling factors ν, if the spin degeneracy is not lifted.

In the beginning of this section the classical description of the $\boldsymbol{E} \times \boldsymbol{B}$ drift has been presented. This drift has to be considered also in the quantum mechanical

picture presented above. The applied electric field $\boldsymbol{E} = (0, E, 0)$ appears in Schrödinger's equation as an electrostatic potential $V(y) = eEy$. The problem can, again be solved in analogy to the harmonic oscillator. However, the center coordinate is now modified to $\tilde{y}_0 = (\hbar k_x + m^* v_\mathrm{D})/eB$, with v_D being the classical drift velocity. The Landau levels are then described by

$$\varepsilon_l(k_x) = \hbar\omega_c\,(l + 1/2) + eE_y\tilde{y}_0 + m^* v_\mathrm{D}^2/2, \tag{35}$$

containing the additional potential term $eE_y\tilde{y}_0$ and the kinetic energy $m^* v_\mathrm{D}^2/2$ from the drift motion. In real space, the additional terms result in a tilt of the Landau levels, as depicted in Fig. 4 (a).

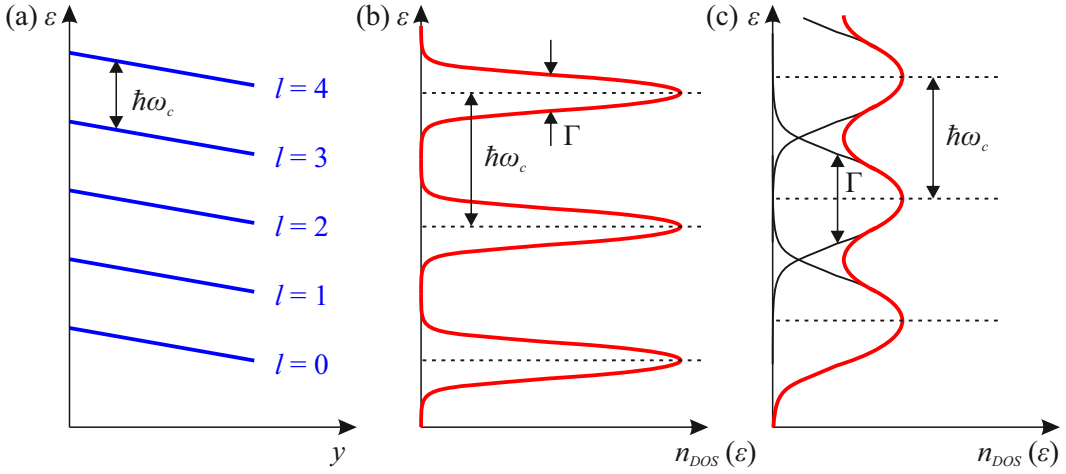

Figure 4: Landau levels in real space representation under application of an electric field E in y-direction are presented in panel (a) and adapted from Ref. [49]. The density of states n_{DOS} in a magnetic field is presented in panels (b) and (c), showing Landau level broadening due to scattering. Distinct Landau levels for $\hbar\omega_c > \Gamma$ in (b) and overlapping Landau levels for $\hbar\omega_c < \Gamma$ in (c). Adapted from Ref. [47].

Generally, the description of the Landau levels as δ-functions is only valid for ideal systems, where scattering, i.e. on other electrons, impurities, or phonons is not present. In real systems at finite temperatures $T \neq 0$, however scattering has to be taken into account. The finite lifetime τ_q defines how long an electron remains unscattered in a system. Note that it differs from the transport lifetime

$\tau_p = \mu m/e$. While all collisions contribute equally to τ_q, the change of direction of the electrons influences the contribution to τ_p strongly.

The finite lifetime τ_q results in an energy uncertainty $\Gamma = \hbar/\tau_q$ for the Landau levels. The precise shape of the real system Landau levels is assumed to be of either elliptic or Lorentzian shape or a combination of both [49]. For all cases, it is important how Γ relates to the Landau level separation $\hbar\omega_c$. For strong magnetic fields $\hbar\omega_c > \Gamma$, the Landau levels are separated and quantum mechanical effects have to be taken into account, see Fig. 4 (b). For low fields the Landau levels overlap and the density of states can be attributed as constant with a periodic modulation, see fig 4 (c). Experimentally this periodic oscillation can, for instance, be observed as 1/B periodic oscillations of the longitudinal magnetoresistivity $\rho_x x$, called Shubnikov-de Haas (SdH) oscillations.

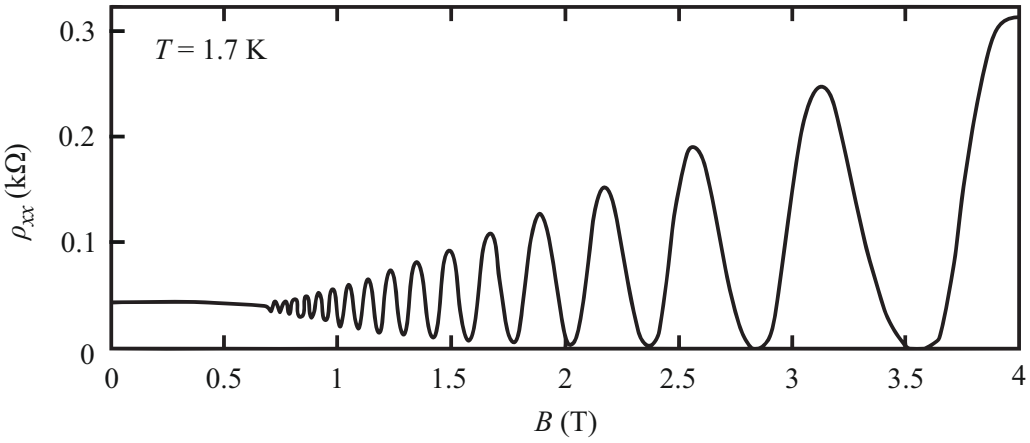

Figure 5: Shubnikov-de Haas oscillations in the longitudinal resistivity ρ_{xx} of a 2DEG in a 10 nm GaAs quantum well. The measurement was performed at the temperature $T = 1.7\,\mathrm{K}$. Adapted from [49].

The longitudinal resistivity in the low-magnetic-field SdH-regime is given by [49]

$$\rho_{xx}(B,T) = \frac{m^*}{n_e e^2 \tau_p}\left[1 - 2e^{-\pi/\omega_c\tau_q}\frac{2\pi^2 k_\mathrm{B}T/\hbar\omega_c}{\sinh(2\pi^2 k_\mathrm{B}T/\hbar\omega_c)}\cos\left(2\pi\frac{hn_e}{2eB}\right)\right]. \quad (36)$$

This equation can be interpreted by looking separately at its components. The magnetoresistance oscillates $1/B$-periodically around the B-independent classical Drude resistivity, which is given by the prefactor. The term in the brackets represents the low-magnetic-field thermodynamic density of states for the broadened LL. It is assumed that the broadening is of Lorentzian shape. Consequently, the oscillatory behavior of the longitudinal resistivity reflects at low magnetic fields the density of states at the Fermi energy. The exponential Dingle factor takes into account the finite lifetime broadening of the LL. For low magnetic fields the separation of the LL $\hbar\omega_c$ is much smaller than the broadening Γ and the modulation amplitude gets strongly reduced. The energy averaging over $k_\mathrm{B}T$ around the Fermi level leads to a reduction of the SdH oscillations' amplitude by temperature. The Fermi energy is assumed to be constant here. For higher magnetic fields this approximation is not valid, since the Fermi energy jumps when the modulation of the density of states is strong or a regime of separated LL is reached [49]. As Eq. 36 shows, the electron density n_e, as well as the quantum lifetime τ_q can be determined from SdH oscillations observed in transport experiments.

2.2 Radiation Induced Effects in Two Dimensional Electron Gases

In the previous section the band structure of a 2DEG and the transport phenomena in crossed electric and magnetic fields are discussed. The physics of such a system exposed to electromagnetic waves are in the focus of the following section. Cyclotron resonance (CR) and electron gas heating are discussed in the first two subsections followed by the core topic of this thesis, microwave induced resistivity oscillations in the third subsection.

2.2.1 Cyclotron Resonance

The effect of cyclotron resonance describes the resonant absorption of radiation with an angular frequency $\omega = \omega_c$ by carriers moving on a cyclotron orbit in a magnetic field B. The x-y-plane is defined as the plane of movement in this section. The phenomenon of CR can be approached either quantum

mechanically as resonant absorption between the Landau levels [50] or classically [51, 52]. Here the classical approach is used. As described in Sec. 2.1.2 electrons are driven on cyclotron orbits by the Lorentz force due to a perpendicular magnetic field. When radiation with an electric field, lying in the cyclotron orbit plane and an angular frequency $\omega = \omega_c$ is incident on the material, it is resonantly absorbed by the moving electrons. The equation of motion of the electrons is

$$m^* \frac{\mathrm{d}\boldsymbol{v}}{\mathrm{d}t} = e(\boldsymbol{E} + \boldsymbol{v} \times \boldsymbol{B}) - \frac{m^* \boldsymbol{v}}{\tau_p}, \tag{37}$$

with the effective mass m^* of the electron in the semiconductor, the carrier drift velocity $\boldsymbol{v}$, the electron charge e, the electric field $\boldsymbol{E}$, the magnetic field strength $\boldsymbol{B}$, and the momentum lifetime τ_p [52]. The current density components can be expressed as $j_i = nev_i$ using the carrier density n_e and $i = x, y$. The absorbed energy density per unit time P is obtained from the Joule losses formula

$$P = \overline{\mathrm{Re}(\boldsymbol{J}) \cdot \mathrm{Re}(\boldsymbol{E})} = \frac{1}{2}\mathrm{Re}(\boldsymbol{J} \cdot \boldsymbol{E}^*), \tag{38}$$

with Re denoting the part of a complex number. Equation (38) shows that the orientation of the electric field of the incident electromagnetic wave is of special importance for the energy transfer. In this thesis the focus lies on circularly right- and left-handed polarized radiation, which will be elaborated on in the following. The radiation is assumed to be propagating along z-direction with an angular frequency ω. For right-handed circular polarization the electric field vector acts as

$$\begin{pmatrix} E_x \\ E_y \end{pmatrix} = \begin{pmatrix} E_0 e^{i\omega t} \\ -iE_0 e^{i\omega t} \end{pmatrix} = E_x \begin{pmatrix} 1 \\ -i \end{pmatrix}. \tag{39}$$

The absorbed power density per unit time for this polarization then reads as

$$P = \frac{\sigma_0 E_0^2}{(\omega + \omega_c)^2 \tau_p^2 + 1}. \tag{40}$$

For left-handed circular polarization the electric field vector is given by

$$\begin{pmatrix} E_x \\ E_y \end{pmatrix} = \begin{pmatrix} E_0 e^{i\omega t} \\ iE_0 e^{i\omega t} \end{pmatrix} = E_x \begin{pmatrix} 1 \\ i \end{pmatrix} \tag{41}$$

and consequently, the power density is

$$P = \frac{\sigma_0 E_0^2}{(\omega - \omega_c)^2 \tau_q^2 + 1} \tag{42}$$

which only defers from Eq. 40 by the sign in the bracket. Remember, that the cyclotron frequency is defined as $\omega_c = eB_z/m^*$, which means that cyclotron resonance for right-handed helicity only occurs if the incident electromagnetic wave moves parallel to the magnetic field vector and for left-handed helicity only when the magnetic field is turned into the opposite direction of the incoming electromagnetic wave. This is a specific characteristic for the case of circularly polarized light. The helicity at which cyclotron resonance absorption occurs for a given magnetic field direction is addressed as CR active (CRA) polarization, whereas the one with no absorption is addressed as CR inactive (CRI). For linearly polarized radiation CR occurs in both magnetic field directions [52]. CR studies are usually carried out in absorption experiments. Under ideal conditions the transmission signal drops to zero for circularly polarized radiation and to ≈ 50 % for linear polarization at the CR magnetic field position B_{CR}. By fitting the slope of the CR-absorption signal with a Lorentzian the momentum relaxation time τ_p can be extracted as the full width at half minimum. However, CR can also be observed in conductivity measurements. In order to evaluate how the absorbed power impacts the conductivity, the conductivity tensor elements from Eq. (20) have to be changed to [53]

$$\sigma_{xx} = \sigma_{yy} = \frac{e^2 n_e \tau_p}{m^*} \frac{\tau_q^{-1} + i\omega}{(\tau_p^{-1} + i\omega)^2 + \omega_c^2}$$

$$\sigma_{xy} = -\sigma_{yx} = \frac{e^2 n_e \tau_p}{m^*} \frac{\omega_c}{(\tau_p^{-1} + i\omega)^2 + \omega_c^2}. \tag{43}$$

Note, that for simplicity an energy distribution of the electrons is not taken into account here and that for $\omega = 0$ the above equations equal the original tensor elements, see Eq. (20). For right-handed circular polarization the conductivity is given by [53]

$$\sigma_+ = \frac{\sigma_0 \tau_p^{-1}}{\tau_p^{-1} + i(\omega + \omega_c)}, \tag{44}$$

and for left-handed circularly polarized radiation as [53]

$$\sigma_- = \frac{\sigma_0 \tau_p^{-1}}{\tau_p^{-1} + i(\omega - \omega_c)}. \tag{45}$$

2.2.2 Electron Gas Heating

The previous section is devoted to the CR and it is shown that it also influences the conductivity σ. In the following the effect of electron gas heating is discussed, which can affect the conductivity strongly, especially if the incident radiation has a high intensity I.

The carriers in an electron gas permanently exchange energy with the lattice. If additional energy is delivered to the electrons it is transfered to the crystal by exchange mechanisms such as electron-phonon scattering. For high temperatures these transfer mechanisms are so effective, that the electrons are considered to be in thermal equilibrium with the lattice. At low temperatures, however, the coupling between charge carriers and the crystal can be much weaker. When the electrons exchange energy very effectively among each other, i.e. that the electron-electron interaction time τ_{ee} is much shorter than the energy relaxation time, their distribution can be described by an effective temperature T_e which is higher than the lattice temperature T_l [54]. This is particularly the case at high carrier densities n_e [55].

The change of carrier energy distribution by incident radiation results in a change of mobility and accordingly a variation of the sample conductivity. The balance equation

$$\frac{K(\omega)I\varepsilon_{eff}}{\hbar\omega} = \langle Q(T_e)\rangle_n \tag{46}$$

determines the electron temperature T_e based on the relation between absorbed energy and the energy loss rate $\langle Q\rangle = \langle d\varepsilon/dt\rangle$. The absorbed energy depends on the absorption coefficient $K(\omega)$, the intensity I and ε_{eff}, which is the effective energy that one photo-excited electron contributes to the system [55].

As mentioned above the increase in T_e leads to a change in mobility μ. The associated conductivity modification is referred to as μ-photoconductivity and described by the equation [55]

$$\frac{\Delta\sigma}{\sigma} = \frac{1}{\mu}\frac{\partial\mu}{\partial T_e}\bigg|_{T_e=T_l} \Delta T_e. \tag{47}$$

In GaAs quantum wells high intensity THz excitation can lead to strong saturation effects [56, 57] of the photoconductivity due to scattering with longitudinal optical (LO) phonons. The energy transfer rate $\langle Q\rangle$ in this case is exponentially dependent on T_e [55], given by

$$\langle Q\rangle = \frac{\hbar\omega_{\mathrm{LO}}}{\tau_{\varepsilon,\mathrm{LO}}} \exp\left(-\frac{\hbar\omega_{\mathrm{LO}}}{k_B T_e}\right). \tag{48}$$

Here the growing number of electrons, which are energetic enough to emit LO-phonons of the energy $\hbar\omega_{\mathrm{LO}}$ lifts the electron-gas temperature and consequently $\langle Q\rangle$. The emission rate is denoted as $\tau^{-1}_{\varepsilon,\mathrm{LO}}$. In comparison to the LO-phonon emission rate of the electrons, the anharmonic decay rate for LO phonons is slow. Hence the energy transfer from electrons to phonons can produce a number of non-equilibrium phonons which results in a saturation of $\Delta\sigma/\sigma$ at high I.

Not only the mobility μ is affected by the electron gas temperature. It was shown in Sec. 2.1.2, that the quantum lifetime τ_q is significantly changed when the lattice temperature T_l is increases, resulting in a decline in SdH oscillation amplitude. The same effect can also be observed, when due to

high intensity illumination the electron gas is heated, which is reasonable considering that the main mechanism limiting τ_q in high mobility 2DEGs is electron-electron scattering [58]. However, it has to be addressed that the effect is weaker for rising T_e as for T_l, since less phonons are involved in the first case. The reduction of the SdH oscillation amplitude is also measured as photoconductivity oscillations under illumination with high intensity radiation. The oscillations occur at the same magnetic field values as the SdH oscillations obtained in magnetotransport experiments.

2.2.3 Microwave Induced Resistivity Oscillations

In the previous sections two photoconductivity effects based on different microscopic mechanisms are discussed. Zudov *et. al* reported on a completely new photoconductivity phenomenon in 2001 [14]. By applying microwave radiation to high mobility ($\mu \geq 3.0 \times 10^6\,\mathrm{cm}^2/\mathrm{Vs}$) GaAs 2DEGs, oscillations of the longitudinal conductivity are observed at low magnetic field values, where contributions of CR and SdH oscillations are not expected. By using ultra high ($\mu \approx 1.5 \times 10^7\,\mathrm{cm}^2/\mathrm{Vs}$) mobility 2DEGs in 2002 Mani *et al.* where able to increase the oscillation amplitude such strongly that they where able to observe zero resistivity states [15]. Both publications attracted a lot of interest and stimulated a high number of works on the topic of MIRO in the following decade.

The original results of Zudov *et al.* are presented in Fig. 6, showing oscillations that are, just like the SdH oscillations, $1/B$ periodic and hence where called "SdH-like"[14]. However, they occur at much weaker magnetic fields, where the Landau levels are not yet strictly separated. Their period is governed by the ratio of $\epsilon = \omega/\omega_c \propto 1/B$, with ω being the microwave frequency and ω_c being the cyclotron frequency. Figure 7 (b) shows MIRO as a function of ϵ. The maxima ϵ^+ and minima ϵ^- are roughly symmetrically offset from the harmonics of the cyclotron resonance at integer ϵ and occur at

$$\epsilon^{\pm} = \epsilon \mp \varphi. \tag{49}$$

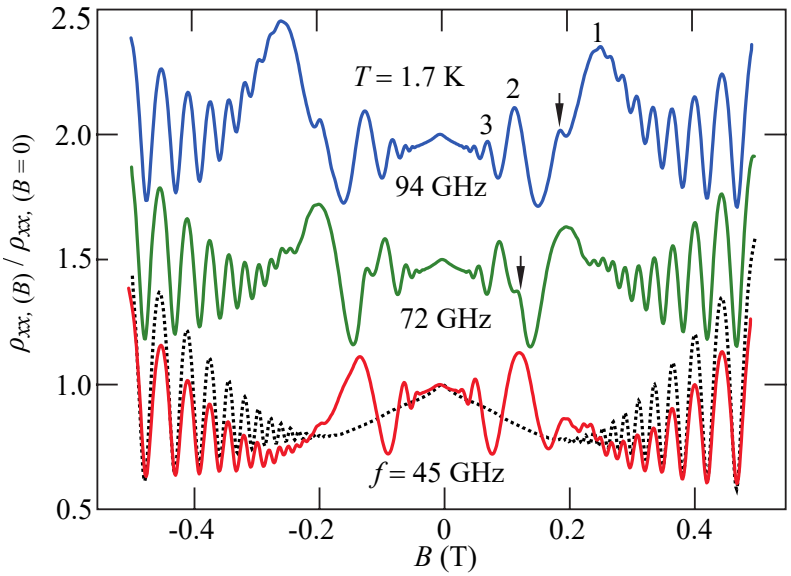

Figure 6: Magnetoresistivity $\rho_{xx,B}$ with (solid lines) and without (dashed lines) microwave illumination for different frequencies $f = 45$, 72, and 94 GHz normalized to its zero magnetic field strength value $\rho_{xx,B=0}$. Data for different frequencies are vertically offset for better visibility. Integer numbers denote maxima corresponding to the order of MIRO ϵ^+. The data is obtained at $T = 1.7$ K in a Hall bar sample. Adapted from [14].

The value of the phase is reported as $\varphi = 1/4$ in many experiments [17–19]. For low harmonics, measurements show that the extrema move towards integer ϵ yielding a phase smaller than 1/4 [21, 25, 27]. The magnetic field dependence of the photoresistivity is described by the empirical equation [10]

$$\Delta\rho = -A_\epsilon \epsilon \sin(2\pi\epsilon) \exp(-\alpha\epsilon), \tag{50}$$

see Fig. 7. Here, the damping parameter α is proportional the inverse of the quantum lifetime τ_q. The experimental oscillation amplitude A_ω is B-independent for $\epsilon \gtrsim 2$. Both α and A_ω are decreasing for increasing temperature [26, 28], hence the majority of experiments on MIRO are performed at or below liquid helium temperature.

It is reported that, at low microwave intensities, A_ω is linear in the radiation's power P [20, 30], but there are also experiments which show a sublinear

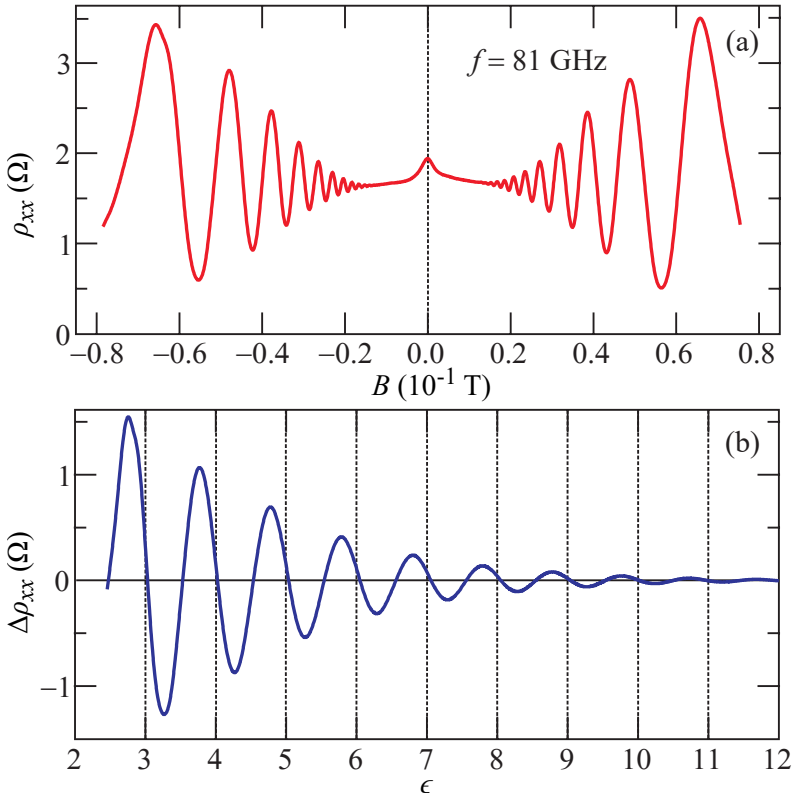

Figure 7: (a) Magnetoresistivity oscillations in respect to B at $f = 81\,\mathrm{GHz}$. Longitudinal resistivity change $\delta\rho_{xx}$ induced by microwave radiation as a function of $\epsilon = \omega/\omega_c$, obtained by subtracting the varying background. The data are obtained at $T \approx 1.5\,\mathrm{K}$ in a Hall bar sample. Adapted from [10].

dependence [24, 31]. Hatke *et al.* showed that, with increasing power there is a cross over from a linear $A_\omega \propto P$ to a sublinear regime $A_\omega \propto P^{1/2}$, accompanied with a decrease of the phase φ [29].

Most of the experiments on MIRO employ frequencies between 30 and 150 GHz [10]. The linear dependence on ω, see Eq. (50), reduces the magnetic field positions of the oscillations for lower excitation frequencies and the oscillations are suppressed by the Dingle factor [10]. For higher frequencies than 150 GHz, however, the amplitude decreases as well [26]. According to theory [42, 46], for fixed $\epsilon \geq 2$ and microwave intensity I the oscillation amplitude scales as $\Delta\rho_{xx} \propto \omega^{-4}$. Nevertheless there are also works reporting on the observation of MIRO-like oscillations induced by terahertz radiation [36, 37].

Apart from many experimental works dedicated to MIRO, several microscopic theories describing the effect have been developed. In general one can separate between mechanisms describing MIRO as an effect originating on the boundaries of the sample, e.g. by Chepelianskii and Shepelyansky [38] or by Mikhailov [39], and so called bulk mechanisms as the displacement mechanism, firstly proposed by Ryzhii *et al.* [40, 59], and the inelastic mechanism which is suggested by Dmitriev *et al.* [41, 42].

2.2.4 Displacement Mechanism and Inelastic Mechanism

Later, in Sec. 4.2 of this thesis it is demonstrated, that the observed oscillations are of bulk nature and the results are analyzed in the framework of the displacement and inelastic mechanism. In this section here a brief introduction to the two mechanisms is given.

Both mechanisms are based on the combination of disorder broadened LL and external magnetic fields affecting either the momentum relaxation in the displacement mechanism or the energy distribution of the electrons within the LL in the inelastic mechanism [10, 46]. The dissipative current $\boldsymbol{j} = en_e(\partial_t \boldsymbol{R})$ is described as a scattering induced shift of the guiding center $\Delta\boldsymbol{R} = R_c \boldsymbol{e_z} \times (\boldsymbol{n}_{\varphi_x} - \boldsymbol{n}_{\varphi'_x})$ where $\boldsymbol{n}_{\varphi_x} = (\cos(\varphi_x), \sin(\varphi_x))$ is the unit vector in direction of motion before the collision and $\boldsymbol{n}_{\varphi'_x}$ afterwards. Here, $R_c = v_F/\omega_c$ is the cyclotron radius with the Fermi velocity v_F. Note that here φ_x does not denote the phase of MIRO φ from Sec. 4.1, but the angle between the direction of the applied electric field and the electron movement direction. The cyclotron orbit shift is sketched in Fig. 8 (a).

In order to describe MIRO, the photoinduced shift ΔX and the resulting current j_x along the x-axis for a homogeneous 2DEG subjected to a dc electric field $\boldsymbol{E} = \boldsymbol{e}_x E$ has to be determined. The shift current has two components $j_x = j_x^{\text{dis}} + j_x^{\text{in}}$ described by the respective mechanisms and resulting in a photoconductivity signal.

At low magnetic fields Landau quantization leads to a periodic modulation of the density of states $n_{DOS}(\varepsilon) \approxeq n_{DOS}(\varepsilon + \omega_c)$. The electric field adds an

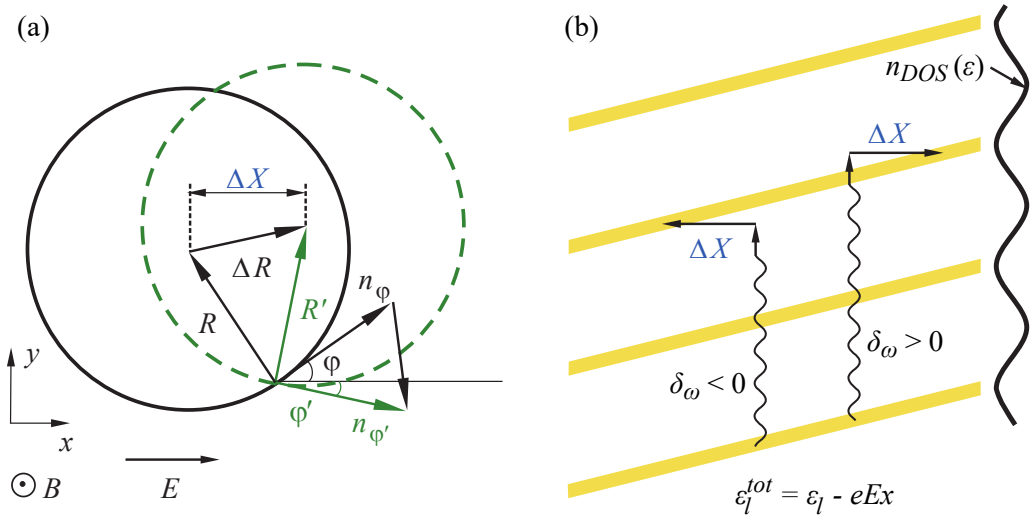

Figure 8: (a) Scattering induced guiding center shift ΔX of a cyclotron orbit. (b) Direction of the shift due to the detuning $\delta_\omega = \omega/\omega_c - N$ for the second harmonic ($N = 2$) of the CR. The yellow stripes represent the LL maxima. Adapted from [10].

electrostatic potential $\phi(x)$ to the system, which makes the density of states spatial dependent, given by

$$\tilde{n}_{DOS}(\varepsilon, x) = n_{DOS}(\varepsilon - e\phi(x)). \tag{51}$$

The normalization to the constant density of states $n_{DOS}(\varepsilon)|_{B=0}$ makes $\tilde{n}_{DOS}(\varepsilon, x)$ dimensionless.

The shift current density is defined as

$$j_x = 2\, n_{DOS}(\varepsilon)|_{B=0}\, e \int_{-\infty}^{x} dx_1 \int_{x}^{\infty} dx_2 (W_{x_1 \to x_2} - W_{x_2 \to x_1}), \tag{52}$$

in terms of the of the probabilities $W_{x_1 \to x_2}$ and $W_{x_2 \to x_1}$ of the guiding center shifts $x_1 \to x_2$ and $x_2 \to x_1$. The probabilities are given by the integrals over the initial ε_1 and final ε_2 energies of the collision, e. g.

$$W_{x_1 \to x_2} = \left\langle \int d\varepsilon_1 \int d\varepsilon_2 \mathcal{M}^{x_1 x_2}_{\varepsilon_1 \varepsilon_2} \delta(x_1 - x_2 + \Delta X) \right.$$

$$\times \left\{ \Gamma^{(el)}_{\varphi_x\varphi'_x} \delta(\Delta\varepsilon^{\mathrm{tot}}_{12}) + \Gamma^{(ph)}_{\varphi_x\varphi'_x} \sum_{\pm} \delta(\Delta\varepsilon^{\mathrm{tot}}_{12} \pm \omega) \right\} \Bigg\rangle_{\varphi_x\varphi'_x}. \tag{53}$$

Here, $\Delta X = \boldsymbol{e}_x \cdot \Delta\boldsymbol{R} = R_c(\sin\varphi_x - \sin\varphi'_x)$ denotes the x-component of ΔR and the whole term is averaged over the initial and final angles. The delta functions in the second line are an expression for the total energy conservation $\Delta\varepsilon^{\mathrm{tot}}_{12} = \varepsilon_1 - \varepsilon_2 + eE\Delta X = 0$ in the elastic scattering ($\propto \Gamma^{(el)}_{\varphi_x\varphi'_x}$) and its change by $\pm\omega$ in the photon-assisted scattering ($\propto \Gamma^{(ph)}_{\varphi_x\varphi'_x}$). The distribution function is given by

$$\mathcal{M}^{\varepsilon_1\varepsilon_2}_{x_1x_2} = \tilde{n}_{DOS}(\varepsilon_1, x_1)\tilde{n}_{DOS}(\varepsilon, x) f_{\varepsilon_1}[1 - f_{\varepsilon_2}], \tag{54}$$

consisting of the dimensionless density of states $\tilde{n}_{DOS}$ and the non-equilibrium distribution functions f_ε. The elastic scattering rate is given by [60]

$$\Gamma^{(el)}_{\varphi_x\varphi'_x} = \frac{1}{\tau_{\varphi_x-\varphi'_x}} - \frac{P_{\varphi_x+\varphi'_x}}{\tau_{\varphi_x-\varphi'_x}} \sin^2\frac{\varphi_x - \varphi'_x}{2}, \tag{55}$$

and the rate for the photon-assisted scattering by [60]

$$\Gamma^{(ph)}_{\varphi_x\varphi'_x} = \frac{P_{\varphi_x+\varphi'_x}}{2\tau_{\varphi_x-\varphi'_x}} \sin^2\frac{\varphi_x - \varphi'_x}{2}. \tag{56}$$

According to Ref. [61] the collisions are described using a generic disorder model characterized by an arbitrary dependence of the elastic scattering rate

$$\tau^{-1}_{\varphi_x-\varphi'_x} = \sum_{m=-\infty}^{\infty} \tau_m^{-1} e^{im(\varphi_x-\varphi'_x)},\ \tau_m = \tau_{-m}. \tag{57}$$

The dimensionless power $P_{\varphi_x+\varphi'_x}$ of the incident radiation's electric field

$$\boldsymbol{E}_\omega(t) = E_\omega \sum_{\pm} \mathrm{Re}[s_\pm \boldsymbol{e}_\pm e^{i\omega t}], \tag{58}$$

where $\boldsymbol{e}_\pm = \boldsymbol{e}_x \pm i\boldsymbol{e}_y$ and $s_\pm$ is the complex vector of unit length determining the polarization of the field, is given by

$$\begin{aligned} P_\theta &= \mathcal{P} - 2\mathrm{Re}[\mathcal{E}_+ \mathcal{E}_-^* e^{i\theta}], \\ \mathcal{P} &= |\mathcal{E}_+|^2 + |\mathcal{E}_-|^2, \\ \mathcal{E}_\pm &= s_\pm e v_F E_\omega \omega^{-1} (\omega \pm \omega_c)^{-1}. \end{aligned} \tag{59}$$

Note that, here the factor $\mathcal{P}$ is sensitive to the circular polarization helicity. A change of the linear polarization's direction, in contrast only has an effect on the second part of the term describing P_θ. Ohms law is now expressed as

$$j_x = \sigma \langle \tilde{n}_{DOS}(\varepsilon)^2 \rangle_\varepsilon E + \Delta\sigma^{\mathrm{dis}} E + \Delta\sigma^{\mathrm{in}} E. \tag{60}$$

Here, the first term describes the linear dark conductivity and $\langle ... \rangle_\epsilon$ denotes the energy averaging over the period ω_c. The other two terms are radiation induced corrections. The first one ($\propto \Delta\sigma^{\mathrm{dis}}$) originates from the photon assisted displacements in Eqs. (53) and (54) if the non-equilibrium distribution function f_ε is replaced by the equilibrium distribution function, given by.

$$f_\varepsilon^{(T)} = [e^{(\varepsilon-\eta)/T} + 1]^{-1}, \ \partial_x \eta = 0 \tag{61}$$

with the space-independent chemical potential η.

The current density contribution of the displacement mechanism reads now

$$j_x^{\mathrm{dis}} = 2e n_{DOS}(\varepsilon)|_{B=0} \sum_{\pm} \int d\varepsilon (f_\varepsilon^{(T)} - f_{\varepsilon\pm\omega}^{(T)}) \cdot \left\langle \Theta(\Delta X) \Gamma^{(ph)}_{\varphi_x \varphi_x'} \right.$$

$$\times \int_{x-\Delta X}^{x} dx' \tilde{n}_{DOS}[\varepsilon - e\phi(x')]\tilde{n}_{DOS}[\varepsilon \pm \omega - e\phi(x' + \Delta X)] \Big\rangle_{\varphi_x \varphi'_x}, \qquad (62)$$

where the Heaviside function $\Theta(\Delta X)$ imposes the condition $\Delta X > 0$. The only contribution of the electric field to Eq. (62) is the position dependence of $\tilde{n}_{DOS}$. The two terms corresponding to $\varepsilon \pm \omega$ would exactly cancel each other out in the absence of a local electric field $E = \nabla\phi(x)$. The conductivity contribution is given by

$$\Delta\sigma^{\mathrm{dis}} = \sigma_D \frac{\tau_p}{4\tau_*}(\mathcal{P} - \mathrm{Re}[\mathcal{E}_+\mathcal{E}_-^*])\mathcal{R}_1,$$

$$\mathcal{R}_1 = \omega\partial_\omega\langle\tilde{n}_{DOS}(\varepsilon)\tilde{n}_{DOS}(\varepsilon+\omega)\rangle_\varepsilon = -4\delta^2\frac{\pi\omega}{\omega_c}\sin\frac{2\pi\omega}{\omega_c}, \qquad (63)$$

which describes the photoconductivity oscillation contribution, reflecting exactly the periodicity and phase of the observed MIRO. Here, τ_*^{-1} is expressed in terms of the partial contribution to the disorder-induced scattering rate, see Eq. (57) as follows

$$\tau_*^{-1} = 2\langle\tau_\theta^{-1}(1 - cos\theta)^2\rangle_\theta = 3\tau_0^{-1} - 4\tau_1^{-1} + \tau_2^{-1}, \qquad (64)$$

where $\langle..\rangle_\theta$ denotes the averaging over θ. Note that the dimensionless power enters Eq. (63), with both, the helicity dependent part and the contribution which depends on the linear polarization.

If the incoming radiation's energy equals the multiples of the distance between the LL maxima ($\omega = n\omega_c$, $n = 1, 2, 3...$), no shift and consequently, no photoconductivity is present. The magnitude and sign of the photoconductivity depends on the energy detuning, for the Nth harmonic of the CR given by

$$\delta_\omega = \omega/\omega_c - N,\ N = 1, 2, 3... \ . \qquad (65)$$

An excited electron will always take the shortest path to its energetically most favorable spot, which is the maximum of the density of states n_{DOS}, see Fig. 8

(b). The electric potential $\phi(x)$ breaks the symmetry of the system, so for the electron in any case, except for exactly at the n_{DOS} minimum, there is a preferred scattering direction. For radiation energy slightly higher than the distance between two maxima of the density of states n_{DOS}, $\delta_\omega > 0$, the electron scatters to the right, and other way around for a lower energy. Scattering of the electrons in direction of the applied field leads to an enhancement of the dissipative current j_x. In the opposite direction it is reduced. Accordingly, the photoconductivity $\Delta\sigma^{\text{dis}}$ due to the displacement oscillates with ω/ω_c, with a phase $\varphi = \pm 1/4$, not to confuse with the angle φ_x.

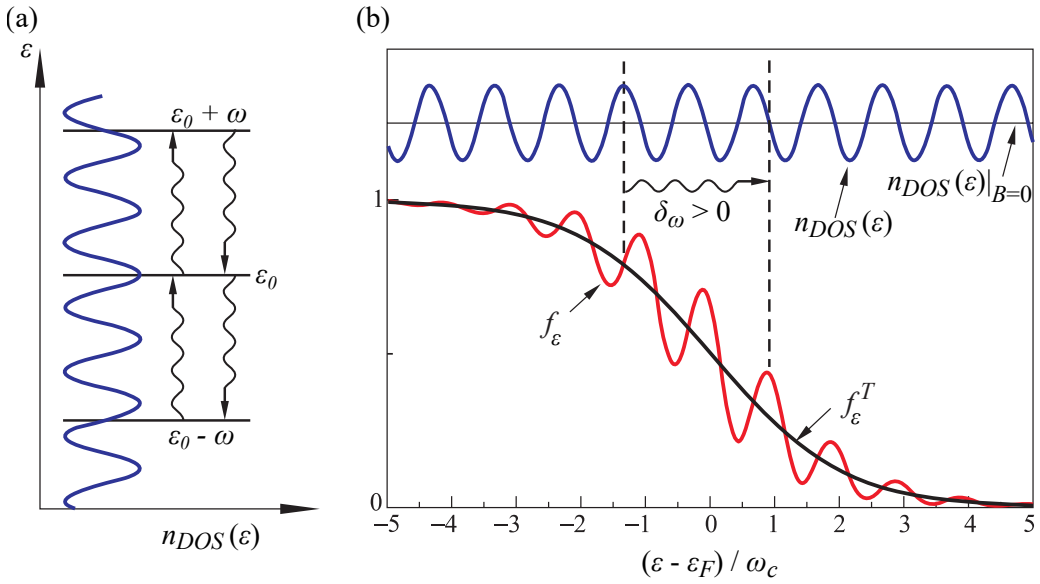

Figure 9: (a) Photon absorption and emission with a detuning of $\delta_\omega = 1/4$. (b) Modulated (blue line) and constant (black line) density of states in phase relation to the equilibrium (black line) and non-equilibrium distribution function (red line). Adapted from [10].

The displacement mechanism assumes an equilibrium electron energy distribution $f_\epsilon = f_\epsilon^T$. The inelastic mechanism, in contrast, takes into account an additional radiation induced change of the energy distribution $\delta f_{\epsilon,x} \propto \tilde{n}_{DOS}(\varepsilon, x)$ [62]. In this model the photoconductivity $\Delta\sigma^{\text{in}}$ depends on the derivative of the distribution function $\partial_\omega \delta f_{\epsilon,x}$.

In contrast to the displacement mechanism, the inelastic mechanism takes into account, that the distribution function f_ε is also influenced by the incoming

radiation. The balance equation for the non-equilibrium energy distribution is given by

$$\frac{f_\varepsilon - f_\varepsilon^{(T)}}{\tau_{in}} = \left\langle \tilde{n}_{DOS}(\varepsilon)^{-1} \Gamma^{(ph)}_{\varphi_x \varphi'_x} \sum_{\pm} (\mathcal{M}^{\varepsilon_2 \pm \omega \varepsilon_1}_{x_2 x_1} - \mathcal{M}^{\varepsilon_1 \varepsilon_2 \pm \omega}_{x_1 x_2}) \right\rangle_{\varphi_x \varphi'_x}, \tag{66}$$

where $\tau_{in} \sim T^{-2}\eta$ is the inelastic relaxation time, describing in which time changes in the distribution function are balanced out. Just as for the displacement mechanism, the a chemical potential η is assumed to be spatially independent here. The photo-induced change to the balance equation reads

$$\delta f_\varepsilon = \mathcal{P} \frac{\tau_{in}}{4\tau_{tr}} \sum_{\pm} (f_\varepsilon^{(T)} - f_{\varepsilon \pm \omega}^{(T)}) \tilde{n}_{DOS}[\varepsilon \pm \omega - e\phi(x)]. \tag{67}$$

Now, the dependence of the density of states on x also leads to an oscillation of δf_ε with space. Consequently, the elastic contribution to the current j_x in Eq. (52) does not vanish, $\mathcal{M}^{\varepsilon\varepsilon}_{x_2 x_1} - \mathcal{M}^{\varepsilon\varepsilon}_{x_1 x_2} \neq 0$.

The inelastic contribution to the current is obtained by substituting Eq. (67) into Eq. (52), reading

$$j_x^{\text{in}} = 2e\, n_{DOS}(\varepsilon)|_{B=0} \int d\varepsilon \left\langle \Delta X \Theta(\Delta X) \int_{x-\Delta X}^{x} dx' \frac{\tilde{n}^2_{DOS}(\varepsilon, x') \nabla_{x'} \delta f_{\varepsilon x'}}{\tau_{\varphi - \varphi'}} \right\rangle_{\varphi\varphi'}. \tag{68}$$

The conductivity contribution, then is given by

$$\begin{aligned} \Delta\sigma^{\text{in}} &= \sigma_D \frac{\tau_{in}}{4\tau_{tr}} \mathcal{P} \mathcal{R}_2(\omega), \\ \mathcal{R}_2(\omega) &= \omega \partial_\omega \langle \tilde{n}_{DOS}(\varepsilon)^2 (\tilde{n}_{DOS}(\varepsilon + \omega) + \tilde{n}_{DOS}(\varepsilon - \omega)) \rangle_\varepsilon. \end{aligned} \tag{69}$$

Just as the displacement mechanism, the inelastic mechanism describes MIRO well in terms of periodicity and phase. The phase comes again from the energy

detuning δ_ω. If it is positive it leads to an increase of the occupation for states lying above a LL maximum, decreasing the number of states below simultaneously. Since the conductivity depends on the derivate of δf_ε, already a small change can have a large impact. Note, that in contrast to the displacement mechanism, the inelastic mechanism is only sensitive to the circular polarization's helicity and not the direction of the linear polarization.

3 Methods

In the following a short description of the probed samples in terms of sample characteristics, such as mobility and carrier density, and the used contact geometries is given. Afterwards the experimental setup will be illustrated.

3.1 Investigated Samples

The two kinds of GaAs/AlGaAs heterostructures probed in this work are explained in this chapter. Additionally the different contact geometries are shown and their respective advantages and disadvantages are illustrated.

3.1.1 Material Properties

In this work (001)-oriented, molecular-beam-epitaxially grown GaAs/AlGaAs quantum wells are probed. All of them have at least one δ-doping layer. These layers are positioned outside the 2DEG and consist of n-donors enhancing the carrier density inside the 2DEG. Two kinds of samples were produced for this work: The samples #A, #D, #E, and #G, which are sketched in Fig. 10 (a), are grown in the group of Prof. Dr. Bougeard and consist of a layer of GaAs, surrounded by two AlGaAs layers with single silicon-δ-doping. The quantum well width of those samples is $d = 10$ nm. The second kind of samples, #B, #C, shown in Fig. 10 (b), were by Dr. N. N. Mikhailov, and Dr. S. A. Dvoretsky in the Rzhanov Institute of Semiconductor Physics in Novosibirsk, Russia. Here the GaAs layer is embedded in alternating layers of GaAs and AlAs that are forming a superlattice. In this case the QW width is $d = 12.5$ nm.

The transport parameters presented in Tab. 1 are obtained at $T = 2\,\mathrm{K}$ on samples contacted in either van-der-Pauw or Hall bar geometry. The photoconductivity measurements that form the main experimental part of this work are performed on samples from the same wavers, but contacted in Corbino disc geometry. Although the majority of works on MIRO were performed on Hall bar samples [10, 14, 15], MIRO and even zero resistant states were observed on Corbino disk samples [16, 63]. Since MIRO only occur in the longitudinal resistance, it is worthwhile to measure the xx-direction

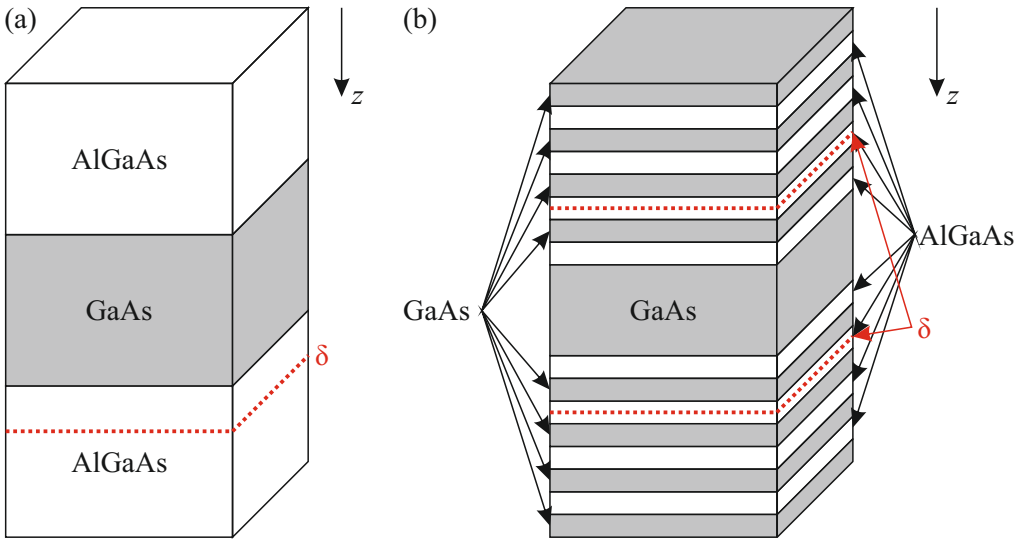

Figure 10: Sketch of the two different types of sample structures probed in this thesis. (a) Double AlGaAs enclosed GaAs heterostructure with single δ-doping. (b) GaAs/AlGaAs superlattice enclosed GaAs QW with double δ-doping.

with highest possible accuracy. This accuracy is not provided if the measured conductivity is influenced by both longitudinal- and Hall-conductivity, e.g. due to misalignment of the sample contacts, which is possible in van-der-Pauw and Hall bar samples. Misalignment is particularly an issue if the samples are large sized, as it is necessary for parts of this work. Therefore Corbino geometry is chosen here, since for this sample geometry, the longitudinal conductivity σ_{xx} can be directly probed, and no Hall contribution is present [49].

As fig. 11 (a) illustrates a Corbino disc consists of a radial inner contact with radius r_i centered in the middle of a larger outer contact ring with radius r_o. For this work the contacts are fabricated as an Au/Ge coating in the group of Prof. Dr. Weiss in Regensburg or, for samples #B and #C, in Novosibirsk. The sample radii are given in Tab. 1. Where multiple radii are shown, multiple samples from one waver with different radii exist, to satisfy specific experimental requirements which are explained in the respective sections of the chapters 4.2 and 4.4. The Corbino disc contacts are evaporated on square shaped samples ranging from five to eleven millimeters side length.

Sample	r_i [mm]	r_o [mm]	μ $10^3\,[\mathrm{cm}^2/\mathrm{Vs}]$	n_e $10^{11}\,[\mathrm{cm}^{-2}]$	QW thickness [nm]
#A	0.25	1.5/4.25	820	12.0	10
#B	0.3	1.0	1800	9.3	12.5
#C	0.3	1.0	150	18.0	12.5
#D	0.25	1.5/4.25	980	24.0	10
#E	0.25	1.5	280	3.7	10
#G	0.5/1.0/1.5	4.25	680	13.5	10

Table 1: Sample parameters and transport data obtained at $T = 2\,\mathrm{K}$ including the electron density n_e and mobility μ.

3.1.2 Corbino Geometry

In this work mainly photoconductivity is measured, which is defined as the difference in conductivity between illuminated and dark sample. When measuring conductivity in a Corbino disk, a significant geometrical influence has to be taken into account. When a voltage is applied between the inner and outer contact, the cylindrical symmetry requires the Electric field lines to point radially outwards. Due to the Lorentz force the current density lines follow logarithmic spirals between the contacts, see Fig. 11 (b). The only current component that is measured is the longitudinal one. Hence, only the σ_{xx} component of the conductivity tensor is accessible, not the horizontal σ_{xy} [49]. The current density at the inner contact is given by $j = I/(2\pi r_i)$ with the electric field strength $E = j/\sigma_{xx} = I/(2\pi r_i \sigma_{xx})$. The voltage difference between inner and outer contact then reads $U = I/(2\pi\sigma_{xx}) ln(r_o/r_i)$[49]. From this, the longitudinal conductivity is given as

$$\sigma_{xx} = \frac{1}{R}\frac{1}{2\pi}\ln(\frac{r_o}{r_i}). \tag{70}$$

Since in this work only the longitudinal conductivity is in focus it will be denoted as σ in the following.

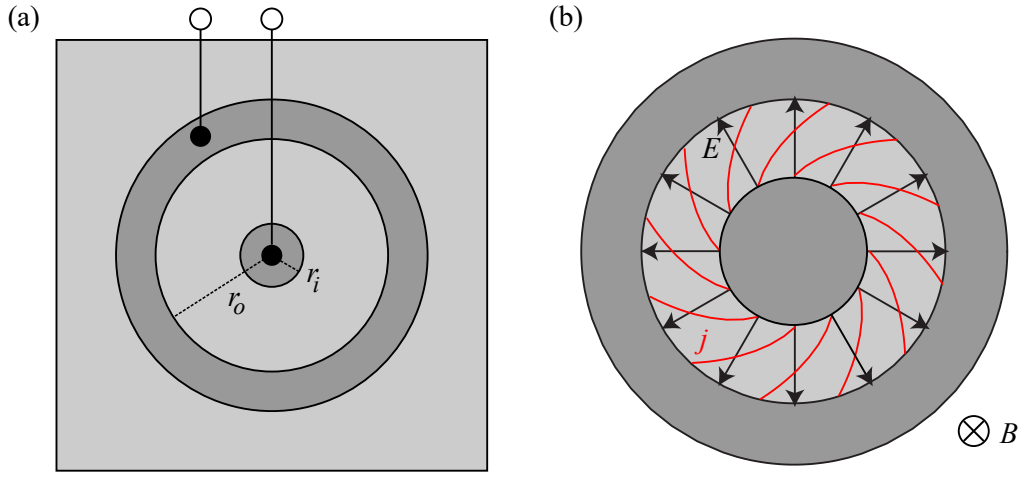

Figure 11: (a) Sketch of the Corbino geometry consisting of two radial contacts. (b) Electric field and current distribution in a Corbino disc with an applied magnetic field. Adapted from [49].

3.2 Experimental Technique

The samples described above are illuminated with monochromatic THz radiation to study the photoconductivity response. In this section the optical and the electrical setup for the photoconductivity experiments are described.

Two types of THz lasers are employed for the experiments in this thesis, a continuous wave (cw) one and a pulsed one. They are pumped by a cw or a pulsed CO_2 laser in turn: The longitudinally excited CO_2 laser, emits cw radiation of a few tens of watts power, and the transversely-excited atmospheric pressure (TEA) CO_2 laser emits short ($\approx$ 100 ns) pulses with powers up to megawatts. Both systems have in common that the emitted radiations wavelength is tunable in the range between 9 and 11 µm. The laser beam is coupled into a .ond resonator, where a molecular gas is pumped to emit THz radiation due to rotational laser transitions. Several discrete THz wavelengths between 35 µm and 496 µm can be achieved by choosing different molecular gases and pumping lines. All lasers emit radiation with a Gaussian transversal profile and a beam diameter between 2 and 3.5 mm full width at half maximum. A detailed description of the laser systems can be found in Ref. [55]. Pulsed laser

wavelengths used in this work are 280, 385, and 496 µm, the cw wavelengths employed are 186 and 432 µm.

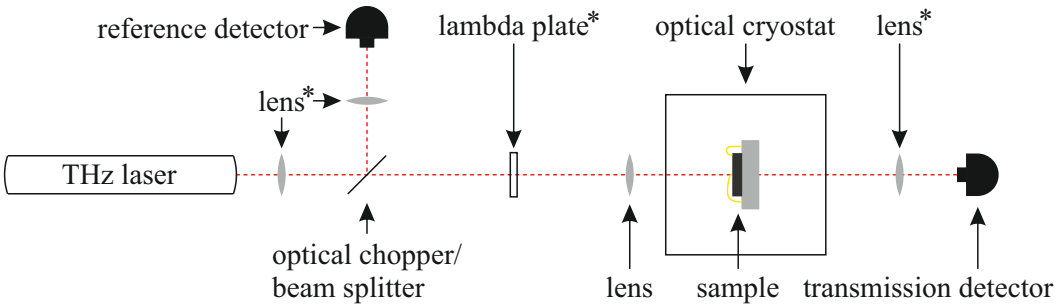

Figure 12: Sketch of the optical setup. The red dotted line represents the beampath. Components marked with a star (*) are optional and only included in the setup if necessary. Depending on the laboratory conditions some lenses are replaced by parabolic mirrors. The optical chopper is used only for the cw setup, consists of aluminum, which reflects THz radiation, and acts similarly to the beam splitter in the pulsed setup.

Figure 12 shows a sketch of the optical setup used for most of the experiments in this thesis. The emitted laser beam is firstly transmitted trough a lens to reduce the divergence of the beam, which is particularly present at the cw laser. Afterwards a part of the signal gets decoupled from the beampath by either a beam splitter (pulsed) or a reflecting chopper (cw) in order to get focused by a lens and detected as a reference signal. Photon drag detectors [55] are used for the pulsed and pyroelectric [55] ones for the cw radiation. The chopper additionally fulfills its usual purpose which is modulating both the probe and the reference beam, to allow lock-in processing of the measured signals. A lambda plate can be included in the setup to manipulate the polarization state of the THz radiation, which is linear when emitted from the gas laser. Before entering the optical cryostat the beam gets focused. Note that the lenses are put in Fig. 12 to keep the sketch simple. In reality most of the focusing is done with parabolic mirrors, which have less signal loss. The sample is fixed on a carrier which is built to transmit as much of the radiation as possible. The electrical connection of sample and holder is realized by gold wires welded on sample- and carrier-gold-contacts. The optical cryostat also includes superconducting magnets which can achieve a field strength $B = 7\,\mathrm{T}$. Radiation which passed

the sample is detected behind the cryostat, which makes a parallel detection of photoconductivity- and transmission/absorption data possible. Transmission signal is picked up by a photon drag detector at the pulsed system and by either a pyroelectric detector or a Golay cell [64] in the cw case.

The photoconductivity data presented in this thesis is detected according to the circuit diagrams presented in Fig. 13. A dc voltage U_{dc} is applied to the sample and a varied magnetic field of field strength B is positioned perpendicular to the sample surface and hence the 2DEG plane. The THz laser beam impacts also normal to the 2DEG plane. The radiation is either pulsed or modulated by a chopper, which means that it changes periodically from zero to maximum intensity. The intensity change results in a conductivity change, which consequently results in a voltage drop via a load resistor of resistance R_L. The voltage drop is detected by a lock-In amplifier in the medium intensity *cw* case or, preamplified by a AD50 amplifier, by a GHz oscilloscope for high intensity pulsed radiation. The AD50 has an amplification factor 100 and a bandwidth of 300 MHz. The high frequency signals are carried by high quality coaxial cables and the open ends are covered by 50 Ω resistors.

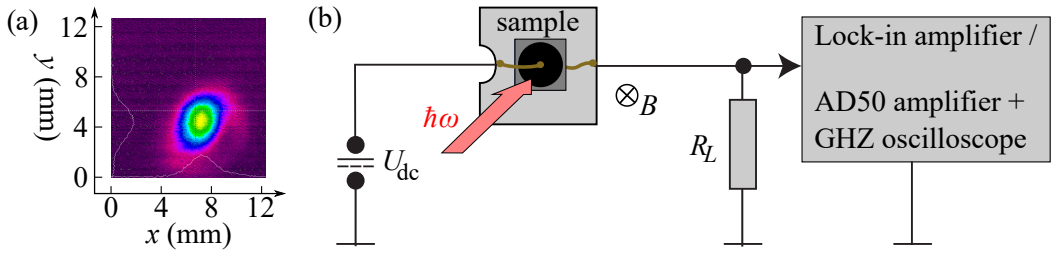

Figure 13: (a) Sketch of the electrical wiring of the photoconductivity setup. The sample is biased by a dc voltage U_{dc}. The the measured voltage drop U_{m} via the load resistor (resistance: R_L) is proportional to the photoconductivity.

When the sample is irradiated the total current reads

$$I = \frac{U_{\mathrm{dc}}}{R_S(B, I_\omega)} = \frac{U_L(B, I_\omega)}{R_L}, \tag{71}$$

where I_ω represents the radiation intensity and R_S is the sample resistance. Solving the equation one obtains

$$R_S(B, I_\omega) = R_L(\frac{U_{\mathrm{dc}}}{U_L(B, I_\omega)} - 1). \tag{72}$$

The voltage drop U_L over the load resistor consists of a dc radiation independent part $U_L(B, I_\omega = 0)$ and an ac part $U_L(B, I_\omega)$ which is induced by the change in conductivity.The dc component, however, is canceled out by either the lock-in amplifier for *cw* or by the oscilloscope for pulsed radiation. Accordingly the measured voltage U_m is proportional to the photoconductivity $\Delta\sigma$:

$$U_m \propto \Delta\sigma. \tag{73}$$

4 Terahertz Radiation Induced Resistivity Oscillations

This chapter is devoted to the presentation and the discussion of the experimental results. In the first subsection photoconductivity oscillations in an external magnetic field are shown and empirically analyzed. It is demonstrated that the observed oscillations are the THz analogue of MIRO. In the second subsection the advantages of THz radiation compared to microwaves are exploited to determine whether the observed effect stems from the samples is a bulk or the boundaries. This helps to identify which microscopic description applies best to the phenomenon. Afterwards the respective microscopic mechanisms are explained in detail. Subsection 4.3 is concerned with the dependence on circular polarization of the MIRO-like oscillations. Thereafter the magnitude of the observed helicity dependence is compared to the theoretical expectations. In the last subsection, 4.4, the chapter is completed by the results of MIRO induced by high intensity THz radiation and the underlying saturation mechanisms.

4.1 Terahertz Analogue of Microwave Induced Resistivity Oscillations

In this subsection photoconductivity measurements under the influence of an external magnetic field are presented. The results are obtained under application of a cw optically pumped molecular THz laser, operating at an average intensity in the range between $I = 10$ mW/cm^2 and $I = 500$ mW/cm^2, depending on the wavelength. It is shown, that the observed conductivity oscillations display the same attributes as MIRO, although being induced by a much higher frequency.

4.1.1 Results

Illuminating a 2DEG under application of a bias voltage and a varying magnetic field, a photoconductivity signal is measured. This photoconductivity $\Delta\sigma$ is exemplary presented in Fig. 14, induced by radiation of the frequency

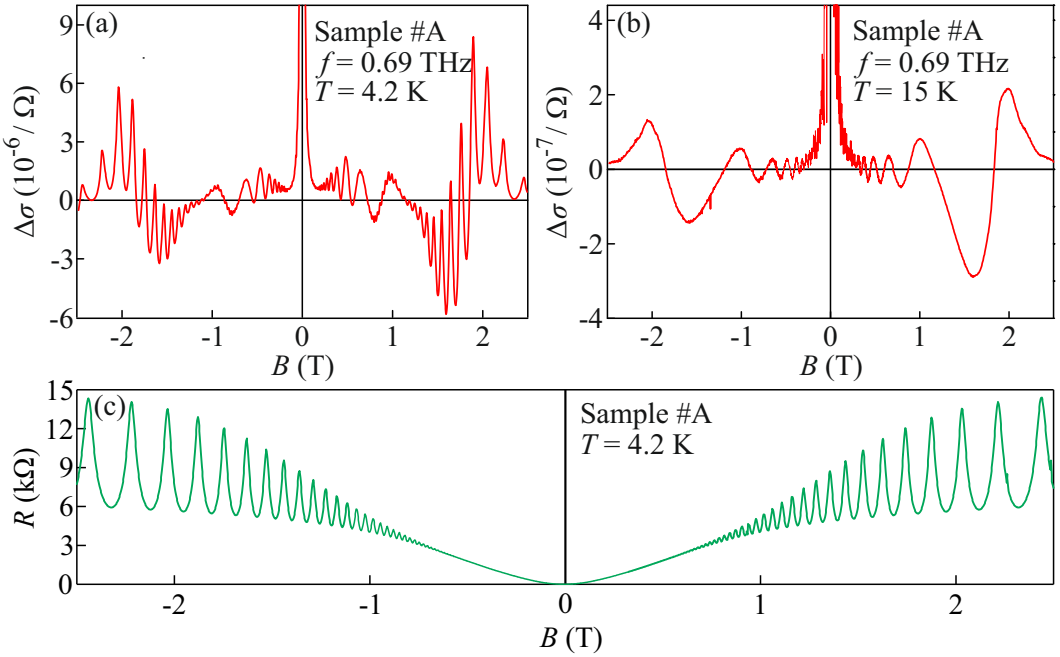

Figure 14: Photoconductivity $\Delta\sigma$ for sample #A induced by modulated cw radiation with the frequency $f = 0.69\,\mathrm{THz}$ and an intensity $I \approx 110\ \mathrm{mW/cm^2}$ as a function of magnetic field B for $T = 4.2$ K in panel (a) and $T = 15$ K in panel (b). (c) Sample resistance R for sample #A in respect to the magnetic field B for $T = 4.2\,\mathrm{K}$.

$f = 0.69\,\mathrm{THz}$ and an intensity $I \approx 110\ \mathrm{mW/cm^2}$ in sample #A. The results are shown for two temperatures, $T = 4.2$ K and $T = 15$ K , in panel (a) and (b), respectively. Strong oscillations of $\Delta\sigma$ are observed, accompanied by a background offset signal, which is particularly strong for low magnetic field values $B \leq 0.2\,\mathrm{T}$. The origin of the background signal is discussed later for normed photoconductivity data. The observed oscillations are symmetric for both magnetic polarities except for the region around $|B| \simeq 1.85$ T. A closer look reveals the presence of two kinds of oscillations, see Fig. 14 (a), both being $1/B$-periodic, but having a different periodicity. The first kind of oscillations are present between $B \simeq 0.25$ T and $B \simeq 2.5\,\mathrm{T}$, whereas the second is present for large magnetic fields, above $B \simeq 1\,\mathrm{T}$. In contrast to this dataset, at higher temperature $T = 15$ K, presented in Fig. 14 (b), only one type is present.

The oscillations present for high magnetic field values, are at the same magnetic field positions as the SdH oscillations observed in dark transport, see Fig. 14

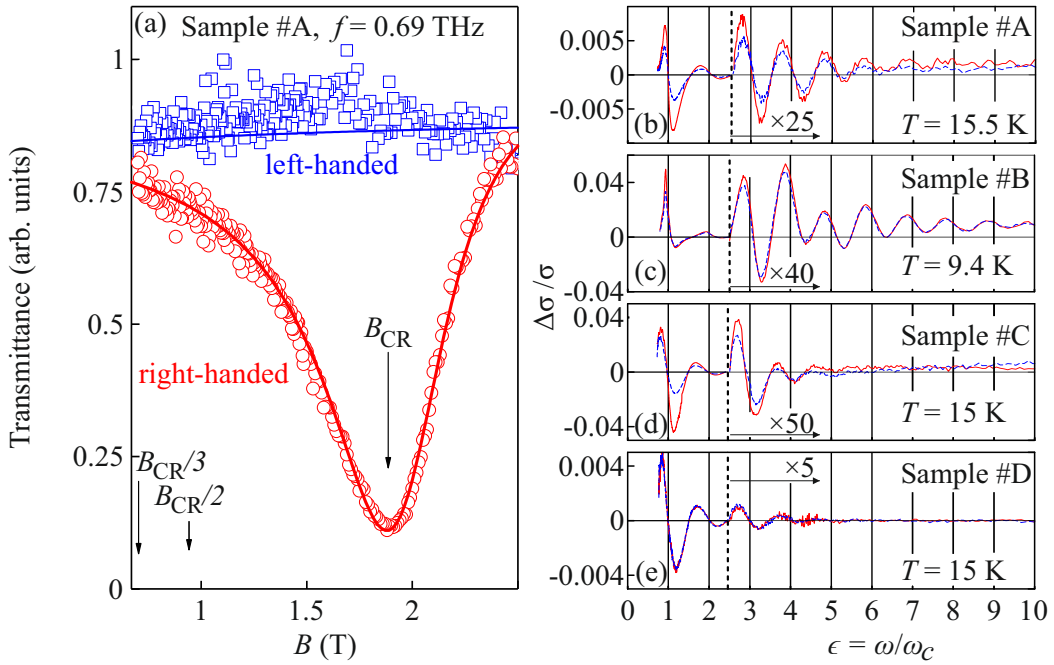

Figure 15: Transmittance as a function of magnetic field B for circularly right- and left-handed polarization shown in (a) as red dots and blue squares, respectively. The lines show transmission calculated after [65]. Panels (b)-(e) show normed photoconductivity $\Delta\sigma/\sigma$ as a function of $\epsilon = \omega/\omega_C$ for four different samples. $\Delta\sigma$ is induced by right- and left-handed circularly polarized radiation, represented by solid red lines and dashed blue lines, respectively. Data for $\epsilon > 2.5$ are magnified by the factors shown in the panels.

(c). The origin of the high B oscillations is discussed in detail in Sec. 4.1.2 and the attention here is put to the first kind of oscillations which is present for $T = 4.2\,\mathrm{K}$ and $T = 15\,\mathrm{K}$ as well. Note that the magnitude of the oscillations is over one order of magnitude smaller for $T = 15$ K, see Fig. 14 (b). Their magnetic field positions, however, are identical in both cases. The oscillation amplitude grows with rising magnetic field B, however there are no more oscillations observed at magnetic fields higher than $|B| \simeq 2.5$ T. Actually, the last and largest pair of extrema has its node at $|B| \simeq 1.88$ T, which is the CR position B_{CR}. The CR position B_{CR} at $\omega = \omega_c$ is obtained from transmission experiments, executed together with the photoconductivity experiments, as described in Sec. **??**. An exemplary dataset for sample #A is shown in Fig. 15

(a). Here, the vertical arrows mark the positions of the first three harmonics of the CR, $\epsilon = \omega/\omega_c = 1, 2, 3$. The transmission data for linearly right-and left-handed circular polarized light is shown as red dots and blue squares, respectively. The solid lines represent fits, which are discussed together with the asymmetric shape of the CR in Sec. 4.3.

The earlier claimed $1/B$-periodicity is much clearer recognizable when the normed photoconductivity $\Delta\sigma/\sigma$ is presented in respect to the oscillation number ϵ, see Fig.15. This number, in turn, is proportional to the inverse magnetic field $\epsilon = \omega/\omega_c \propto 1/B$. The data shown are obtained with four different samples, all illuminated by radiation of the frequency $f = 0.69\,\mathrm{THz}$. The sample temperatures are chosen such, that only the first type of oscillations are observed. Norming the photoconductivity $\Delta\sigma$ to the dark conductivity σ, the observed background signal becomes B-independent and small compared to the oscillatory component. The background can, hence, be attributed to the influence of the sample shape on the dark conductivity. The photoconductivity data presented in Fig. 15 (b)-(e) clearly show that for the four probed samples, the oscillations are periodic in ϵ. The extrema are roughly symmetrically offset to ϵ. Moreover, in all four cases the oscillation amplitude reduces with rising ϵ. The magnitude of the amplitude damping depends on the sample.

The amplitude of the observed oscillations depends linearly on the radiation's power. Reducing the radiation intensity reduces the amplitude, see Fig. 16 for the photoconductivity in the magnetic field range between $B = 0.3\,\mathrm{T}$ and $B = 0.55$ where oscillations with $\epsilon = 4$ and $\epsilon = 5$ are found. Note that the positions of the extrema do not change. The differences in photoconductivity of the maximum and minimum for each oscillation in respect to the ratio between applied and maximum intensity, I/I_{max}, are shown in Fig. 16 (b), demonstrating a linear intensity dependence.

Changing the excitation frequency from $f = 0.69$ THz to $f = 1.62$ THz modifies the periodicity of the first type, but does bot influence the oscillations with the SdH period. This is shown exemplary for sample # A in Fig. 17 (a). The experiments were carried out at helium temperature and under excitation with either right- or left-handed circularly polarized radiation, represented by the red solid and the blue dashed line, respectively. Note that the radiation

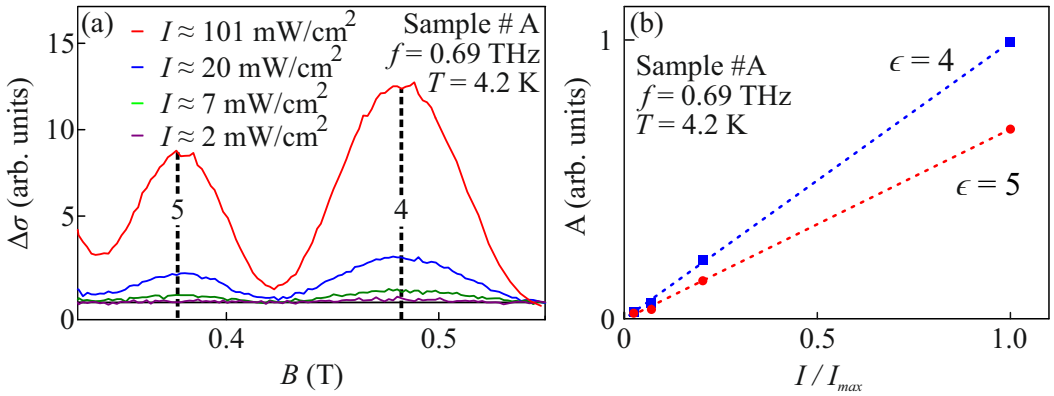

Figure 16: Intensity dependence of the photoconductivity oscillations . Panel (a) shows the magnetic field dependence of $\Delta\sigma$ for four different intensities for $\epsilon = 4$ and $\epsilon = 5$. The intensity dependence of the amplitudes A of the 4th and 5th harmonics is presented in panel (b). The data show that the oscillation amplitude scales linearly with the radiation intensity and that the maximum signal positions do not shift with changing intensity.

intensity at this frequency is by a factor of five larger ($I \approx 550\,\mathrm{mW/cm^2}$) than for the frequency $f = 0.69\,\mathrm{THz}$. The photoconductivity $\Delta\sigma$ is presented in respect to the inverse magnetic field $1/B$. The observed low-B oscillations have a smaller amplitude compared to the lower frequency data and a more unsteady background signal is present. Figure 17 (b) shows the respective transmission data. It reveals that also the CR position has shifted. For an excitation frequency of $f = 1.62$ THz it is found at $B \simeq 4.25$ T.

Note that both, the transmission data as well as the photoconductivity is presented for illumination with circularly right- and left-handed polarized radiation, respectively represented by red- and blue-colored graphs. In contrast to the transmittance, the photoconductivity shows only a weak helicity dependence. This feature is analyzed in detail in Sec. 4.3.

4.1.2 Discussion

The origin of the photoconductivity oscillations in the external magnetic field presented in the previous subsection is discussed in the following. At first, the oscillations, which vanish for higher temperatures are discussed.Secondly,

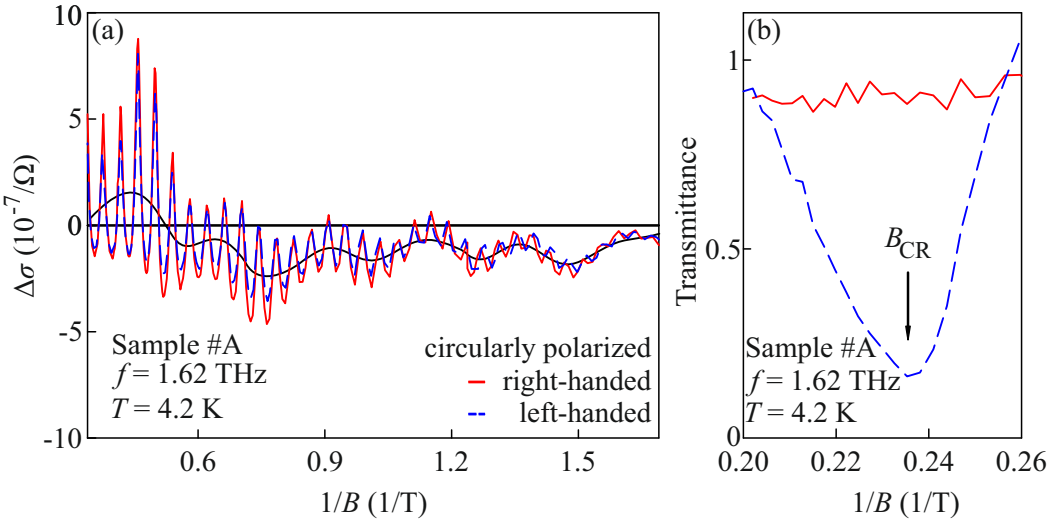

Figure 17: Photoconductivity data $\Delta\sigma$ (a) and transmittance data (b) for sample #A induced by modulated cw radiation with the frequency $f = 1.62\,\mathrm{THz}$ and an intensity $I \approx 550\ \mathrm{mW/cm^2}$ as a function of magnetic field B for $T = 4.2\ \mathrm{K}$.

and in more detail, the temperature resistant oscillations, which occur at lower magnetic field values are discussed. Therefore, the shape of the normed photoconductivity signal is analyzed and empirically fitted. A particular focus lies on the oscillation amplitude A_ϵ, the phase φ, which separates the oscillation extrema from the node positions ϵ, and the damping parameter α.

Comparing the oscillations in Fig. 14 (a) to the magneto-transport data for this sample presented in Fig. 14 (c) shows, that the photoconductivity oscillations are at the same magnetic field values as the SdH oscillations measured in dark conductivity. Observed only for low temperatures, the second type of oscillations, see Fig. 14 (a) and Fig. 17 (a), can be attributed to a trace of SdH oscillations observed in the photoconductivity signal. They can be attributed to the decrease in SdH-amplitude due to electron gas heating induced by the THz radiation, described in Sec. 2.2.2. The absence of the high B oscillations in the photoconductivity data for $T = 15\,\mathrm{K}$, presented in Fig. 14 (b), supports an explanation based on heating, because an increase of electron gas temperature T_e does not yield a reduction of SdH amplitude at this sample temperature. This is due to the fact, that at this temperature $T = T_l = 15\,\mathrm{K}$ no SdH

oscillations are observed in magneto transport either, due to the smeared out LL, see Sec. 2.1.2.

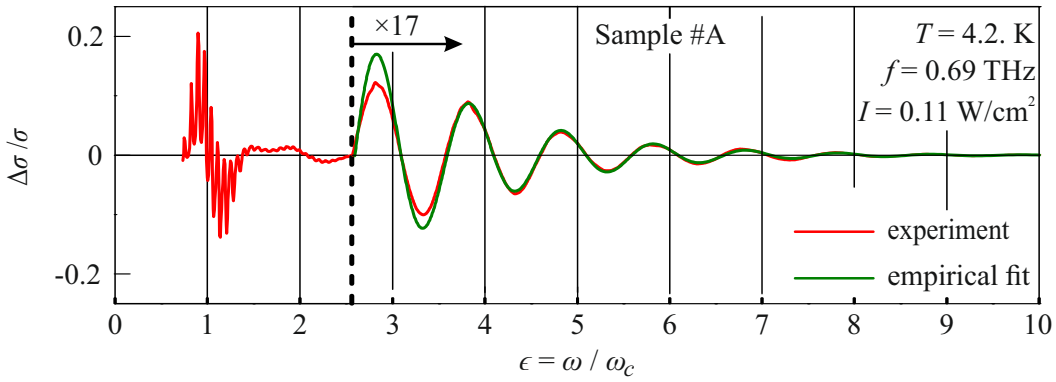

Figure 18: Normed photoconductivity $\Delta\sigma/\sigma$ as a function of ϵ for sample #A at $T = 4.2$ K represented by the red line. For better visibility $\Delta\sigma/\sigma$ has been multiplied by a factor 17 for higher harmonics ($\epsilon \geq 3$) and the B-independent offset is subtracted. The green line is a fit after Eq. (74) with B-independent A_ϵ.

Now the other type of oscillations, present at low magnetic field values $B \leq 2.5\,\mathrm{T}$ are analyzed. Figure 18 shows the normed photoconductivity of sample #A in respect to the oscillation number ϵ measured at $T = 4.2\,\mathrm{K}$, represented by the red line. It is complemented by an empirical fit, given by

$$\Delta\sigma/\sigma = -\epsilon A_\epsilon \sin(2\pi(\epsilon + \delta\epsilon)) \exp(-\alpha\epsilon), \tag{74}$$

represented by the green line. Here A_ϵ is the experimental oscillation amplitude, which shows to be B-independent for $\epsilon > 2$, and α is the exponential damping parameter. The fit can not be applied reliably for lower harmonics. In this range the photoconductivity is influenced additionally by the CR. Similarly to the procedure on photoconductivity oscillations reported in previous works [10, 14] the low harmonics are excluded from the analysis based on Eq. (74). Note that, except for the additional phase $\delta\epsilon$, Eq. (74) is identical to Eq. (50) in Sec. 2.2.3, the empirical fit of MIRO, firstly reported in Ref. [14]. The CR position $B_{CR}^{fit} = 1.84\,\mathrm{T}$, extracted from the fit and therefore based on the periodicity of the oscillations is in good accordance to $B_{CR} = 1.85\,\mathrm{T}$ the value obtained in

the transmission experiments. Table 2 in Sec. 4.2, shows B_{CR}, the additional phase $\delta\epsilon$, the oscillation amplitude A_ϵ and the damping parameter α extracted from the normed photoconductivity $\Delta\sigma/\sigma$ measurements, together with the temperature of the respective experiments.

Due to the exponential damping, higher harmonics, $\epsilon \gg 1$, can not be resolved sufficiently well to allow a precise fit without additional methods. However, the precision for high harmonics can be checked by multiplying the normed photoconductivity $\Delta\sigma/\sigma$ with a part of the empirical fitting term $-\epsilon \exp(\alpha\epsilon)$, as exemplary shown for sample #A in Fig. 19(a). The amplitude now is constant for up to $\epsilon = 12$, showing how good the fit corresponds to the obtained data, even though several parameters are involved.

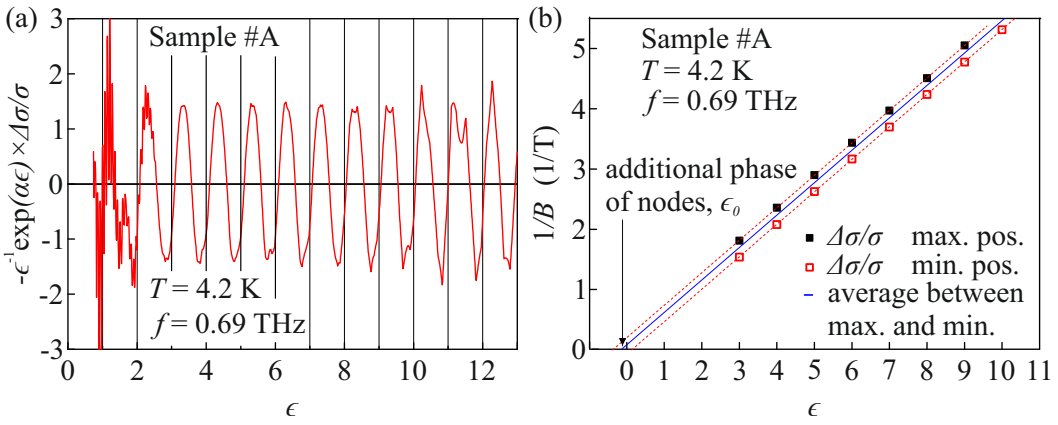

Figure 19: (a) Relative, normed oscillations $\Delta\sigma/\sigma$ with removed constant background when multiplied by $-\epsilon^{-1}\exp(\alpha\epsilon)$ in respect to ϵ. The damping factor α is taken from the fit after Eq. (74). The plot illustrates the quality of the fit in relation to the original data for high harmonics $\epsilon \gg 1$. (b) Example of how B_{CR}, $\delta\epsilon$, and φ are obtained.

From the presented data also the phase φ of the oscillations extrema relative to the nodes can be extracted. The extrema are found at

$$\epsilon^{\pm} = \epsilon \mp \varphi, \tag{75}$$

with the phase being $\varphi = 1/4$ for all probed samples, and $+(-)$ corresponding to maxima (minima). The phase $\varphi = 1/4$ is reported to be universal in

Refs. [17–19]. Figure 19 shows exemplary for sample #A how the phase φ, the additional phase $\delta\epsilon$ and the CR magnetic field position B_{CR} are precisely determined from the photoconductivity data. The $1/B$ values of the magnetic field positions of the oscillation's minima and maxima are plotted against ϵ. From the gradient $1/B_{CR} = 1/1.84\ \mathrm{T}^{-1}$ of the straight lines which are fit through maxima and minima positions the CR position is obtained. Precisely in the middle between the red lines a blue line representing the nodes of the oscillations is placed, which crosses the abscissas at $\delta\epsilon = -0.09$. The horizontal distance between corresponding extrema is 1/2, which means that they are $\epsilon/2$ phase-shifted to each other and symmetrically offset from the nodes by $\varphi = 1/4$.

MIRO amplitude is reported to strongly decline with rising frequency, $A_\epsilon \propto \omega^{-4}$ [10, 26]. Sample #A is probed with the frequency $f = 0.69\,\mathrm{THz}$ in Fig. 15 (a) and the frequency $f = 1.62$ THz in Fig. 17, both at $T = 4.2\,\mathrm{K}$. The oscillation amplitudes are decreased by a factor $F_\omega^{\mathrm{exp}} \approx 5$ for the higher frequency. The ratio of the frequencies $1.62/0.69 \simeq 2.35$ applied to the 4th order frequency dependence of A_ϵ gives a theoretical ratio $F_\omega^{\mathrm{th}} \approx 6$, assuming a linear intensity dependence and considering the five times higher intensity for $f = 1.62\,\mathrm{THz}$. The deviation of both ratios can be explained by the inaccuracy with which the amplitudes for $f = 1.62\,\mathrm{THz}$ are obtained, due to the unsteady background.

The ϵ-periodicity, the exponential damping α, the fixed phase relation $\varphi = 1/4$, and the frequency dependence $A_\omega \propto \omega^{-4}$ are reported as the main experimental characteristics of MIRO, see Sec. 2.2.3. Though being excited by radiation of a higher frequency, the oscillations observed in this work feature all of these characteristics, which shows that they represent the THz analogue of MIRO. The intensity dependence in Fig. 16 supports this assertion. In analogy to MIRO the oscillations are addressed as THz induced resistivity oscillations (TIRO) in the following, although actually conductivity oscillations are presented. Remembering Eq. 23 in Sec. 2.1.2, however, one can conclude that oscillations observed in conductivity are resistivity oscillations at the same time, and vice versa.

4.2 Bulk or Boundary Origin of the Terahertz Radiation Induced Resistivity Oscillations

In the previous section it is shown, that TIRO show the same physical properties as MIRO and hence, are the same effect. The excitation with THz instead of microwaves yields a lot of advantages. The radiation's polarization state can be easier controlled and the laser beam can be focused to a much smaller area than it is possible for a microwave signal. In the following section the latter property is exploited in order to answer one of the most intriguing questions in the hole field of MIRO: Are they an effect excited on the edge between the two dimensional electron gas and the sample boundaries, like contacts or vacuum, or can they also be observed if only the bulk of the sample is illuminated? Answering this question helps to figure out, which of the competing theories for the description of MIRO that developed in the last 15 years can describe the effect. In the beginning of this section the spatial origin of TIRO is determined. Afterwards the microscopic mechanisms, which are in line with the beforehand obtained results are discussed.

4.2.1 Results

To be able to selectively excite the sample large area Corbino discs were manufactured in the group of Prof. Dr. Weiss, with an outer contact diameter of $r_o = 9.5\,\mathrm{mm}$. The, compared to microwaves relatively small spot of the molecular THz laser with a diameter of $d \approx 3.4\,\mathrm{mm}$ full width at half maximum at a frequency of $f = 0.69\,\mathrm{THz}$ is applied to the large sized samples, such, that the sample edges are not illuminated. To guarantee, however, that only the bulk is illuminated, a metal aperture is placed on top of the sample. To avoid boundary effects between aperture and sample, insulating spacers provide a distance between them. A sketch of the aperture on top of the sample is given in Fig. 20 (a). It shows the setup from top perspective and a cut through the sample center along x direction. The laser spot is sketched true to scale. The results of the photoconductivity measurements applied to samples #A and #C as a function of $\epsilon = \omega/\omega_c$ are presented in Fig. 20 (b) and (c), respectively. In both cases well pronounced TIRO are visible, showing all the characteristics

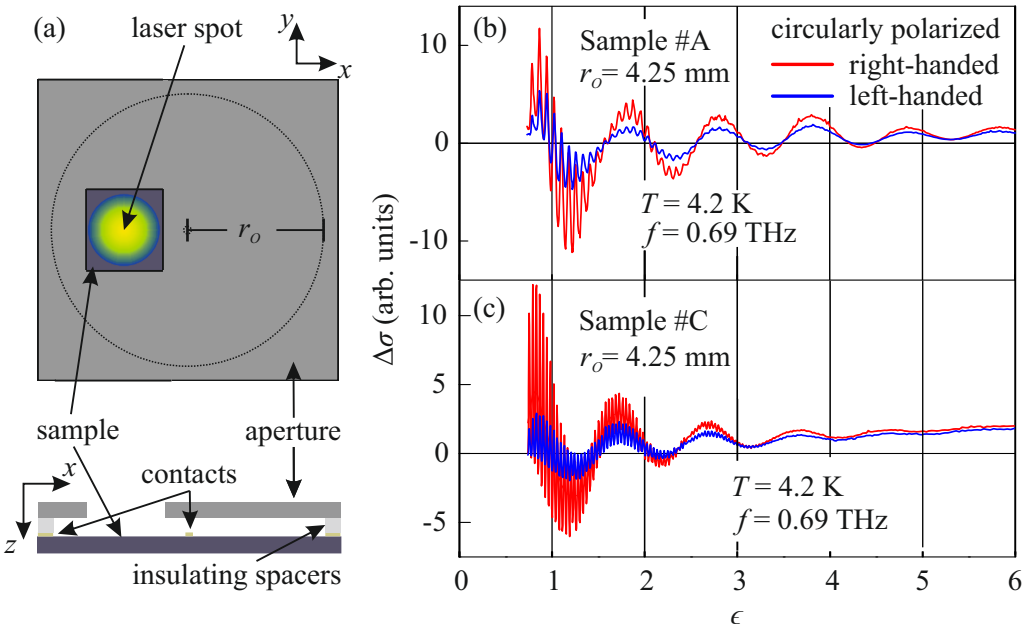

Figure 20: (a) Sketch of the aperture on top of the sample from top view and side view, cut trough the sample center. Photoconductivity $\Delta\sigma$ as a function of ϵ obtained at $T = 4.2\,\mathrm{K}$ with a radiation frequency $f = 0,69\,\mathrm{THz}$ on sample #A and sample #C, presented in panel (a) and (b), respectively.

discussed in Sec. 4.1. Also traces of SdH oscillations are present. The results on the large area samples are consistent with the ones of the small Corbino samples investigated in Sec. 4.1, showing a much stronger exponential decay for sample #C than for sample #A. Both results contain a slightly stronger but still rather weak helicity dependence, with larger oscillation amplitudes for right-handed polarized radiation, which is to be expected since the results for positive magnetic field are presented.

After measuring TIRO without edge illumination, the contacts are now illuminated selectively by scanning the beam outwards from the middle of the sample, where no contacts are, towards the contact region. Therefore, another mask is used, which allows to scan the laser spot from the sample middle towards the edge. This movement of the laser spot along the y-direction from the non-contact area to the contact area of sample #A is illustrated by the inset of Fig. 21. In steps of 0.5 cm the photoconductivity is measured between $B = 0.4\,\mathrm{T}$ and $B = 0.75\,\mathrm{T}$ revealing TIRO with $\epsilon = 3$ and $\epsilon = 5$. The normed

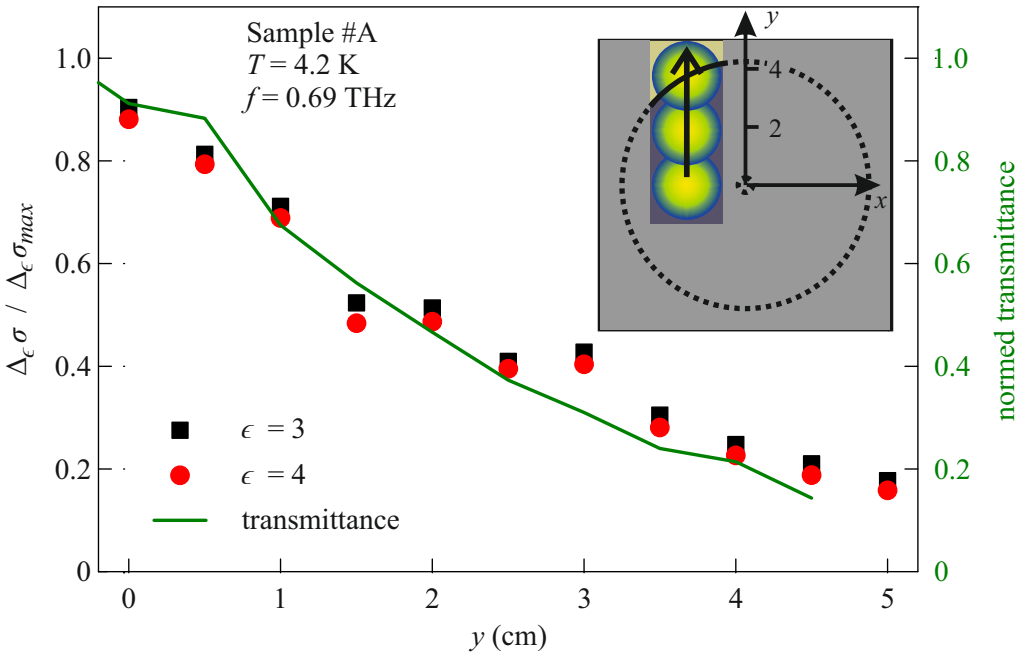

Figure 21: Normed TIRO amplitudes $\Delta_3\sigma/\Delta_3\sigma_{max}$ and $\Delta_4\sigma/\Delta_4\sigma_{max}$ for the third and fourth harmonic, represented by black squares and red dots, respectively. The green line represents the parallel measured transmittance signal normed to its maximum. The variable x represents the positions, were the oscillations, from which the amplitudes are extracted, are measured. The positions are illustrated in respect to the setup geometry by the inset.

amplitudes of the respective oscillations $\Delta_\epsilon\sigma/\Delta_\epsilon\sigma_{max}$ extracted from the photoconductivity measurements, are presented in respect to the beam position y in Fig. 21. Additionally, the transmitted intensity is detected by a large scale Golay cell. Both, the transmission and photoconductivity data are normed to their respective maximum values in order to make it easier to compare their shapes. The presented results are achieved on the large sized sample #A at $T = 4.2\,\mathrm{K}$ excited by radiation of the frequency $f = 0.69\,\mathrm{THz}$ and an intensity I of about $110\,\mathrm{mW/cm^2}$.

The oscillation amplitudes as well as the transmittance signal decrease as the spot moves over the contact edge. The shapes of the three compared datasets are congruent in the limit of the measurement precision.

4.2.2 Discussion

The results presented above approach the question of MIRO origin from two sides. On the one hand photoconductivity is measured with an aperture that prevents edge illumination, and on the other the edge area between sample and contact is selectively irradiated. The first measurement shows, that MIRO must contain a bulk contribution, because the oscillations are well resolved. The stronger helicity dependence for the larger samples are discussed in Sec. 4.3.

With the second experiment a significant edge contribution can be ruled out. If there would be an edge contribution, it would show in a maximum signal when the maximum intensity of the laser spot illuminates the edges. Due to the Gaussian profile of the laser beam, the maximum intensity irradiates the contact edge at $x \approx 4\,\mathrm{cm}$. In this region no significant increase of amplitude is obtained. In general, the oscillation amplitude follows the transmittance signal closely. The transmittance, in turn, is a measure of the intensity I with which the 2DEG is illuminated. The intensity is reduced strongly, due to reflection of the incident radiation by the AuGe contact areas. The linear intensity dependence in the intensity range applied here is discussed in Sec. 4.1. Hence it is not surprising that the normed TIRO amplitudes fit well together with the normed transmittance.

Both experiments separately, but even more in combination show that TIRO is a bulk effect. The two mechanisms describing the phenomenon in that manner are the displacement mechanism, proposed by Ryzhii [59] and the inelastic mechanism, proposed by Dmitriev *et. al* [41, 42]. A phenomenological description of both of them is given in the following oriented on Ref. [10]. For a more detailed discussion of both mechanism see Refs. [10, 61, 62].

Within the theory of the displacement and inelastic mechanism the photoconductivity oscillations are given by [62]

$$\Delta\sigma/\sigma = -\eta\mathcal{P}S_{\pm}\frac{2\pi\omega}{\omega_c}, \tag{76}$$

where the dimensionless radiation power $\mathcal{P}$ and the circular polarization's helicity dependent factor $S_{\pm}$ are given by

$$\mathcal{P} = \frac{2\pi e^2 n_e E_\omega^2}{m^2 \omega^4}, \tag{77}$$

and

$$S_\pm = \frac{|s_\pm|^2}{\gamma^2 + (1 \pm \omega_c/\omega)^2}. \tag{78}$$

The screening factor $|s_\pm| = |E_\pm|^2/E_\omega^2$ takes into account the reduction of the THz field's intensity $|E_\pm|^2$ acting on the 2D electrons compared to the incoming radiation's intensity E_ω^2. The determination of the THz field acting on the 2DEG for the experiments presented in this thesis is presented in the supplementary materials of Ref. [66]. It is based on the analysis of the transmission data separately obtained for each probed sample and takes into account the Fabry-Perot interference due to multiple reflections [65] and superradiant decay [67]. The transmission coefficient $T = |t|^2$, with t being the transmittance amplitude, is used as the fitting function and given by,

$$T_\pm = \frac{\tilde{y}^2 + \gamma^2}{[\tilde{y}^2 + (\gamma + \Gamma)^2]\cos^2\phi + [\tilde{n}^2\gamma^2 + (\tilde{n}\gamma + \Gamma/n)^2]\sin^2\phi - (\tilde{n} - n^{-1})\tilde{y}\Gamma\sin 2\phi},$$

$$\tilde{y} = 1 \pm \frac{\omega_c}{\omega}, \tilde{n} = \frac{n + n^{-1}}{2}. \tag{79}$$

The exact derivation of T can be found in the supplementary materials of Ref. [66]. Two parameters strongly influencing the screening are

$$\gamma = 1/\omega\tau_p, \tag{80}$$

which represents the momentum relaxation in the 2DEG and

$$\Gamma = e^2 n_e / 2\epsilon_0 c m^* \omega, \tag{81}$$

which represents the superradiant decay. Here ϵ_0 is the vacuum permittivity, c the vacuum speed of light, and m^* the effective mass. Whether the Fabry-Perot interference is constructive or destructive, is described by the interference parameter $\phi = nkw$. Here, $n = 3.6$ is the refractive index of the GaAs substrate, $k = \omega/c$ is the vacuum wave vector and w the distance between the sample surfaces. The parameter ϕ can be obtained from the fit of the transmission data. The data for sample #A , which has the carrier density $n_e = 1.25 \times 10^{12}\,\mathrm{cm}^{-2}$ and the mobility $\mu = 82 \times 10^4\,\mathrm{cm}^2/\mathrm{Vs}$, corresponding to $\Gamma = 0.19$ and $\gamma = 0.0065$, is presented in Fig. 15 (a). Since ϕ enters only in trigonometric functions, just the fractional part $\tilde{\phi} = \phi/\phi - \lfloor \phi/\phi \rfloor$ is taken into account. The fit to the data in Fig. 15 (a) then gives $\tilde{\phi} = -0.04$ and $B_{CR} = 1.85\,\mathrm{T}$.

The screening factor entering Eq. (76), can be expressed as a function of T, given by

$$|s_\pm|^2 = |E_\pm|^2/E_\omega^2 = T_\pm(\cos^2\phi + n^{-2}\sin^2\phi). \tag{82}$$

It is shown in Ref. [66] that, for small magnetic field values B and $\gamma, \Gamma \ll 1$, which is valid for the experimental conditions in this thesis, the intensity reduction can vary between $|s \pm|^2 = 1$ for constructive interference and $|s \pm|^2 \sim 0.02$ for destructive interference. The strength of the reduction, depends on the factors:

The factor $\eta = \eta^{\mathrm{in}} + \eta^{\mathrm{dis}}$ in Eq. (76) consists of the 2DEG parameters, influencing how strongly the inelastic and displacement mechanism respectively contribute to the observed oscillations. The inelastic contribution, given by

$$\eta^{\mathrm{in}} = \frac{2\tau_{\mathrm{in}}}{\tau_p} \simeq \frac{2\pi\hbar^3 n_e}{m\tau_p T^2}, \tag{83}$$

includes $\tau_{\mathrm{in}}^{-1} \propto T^2$, the rate of inelastic electron-electron collisions. In contrast, elastic scattering fully determines the rate η^{dis} of the displacement contribution. It is highly sensible to the correlation properties of disorder and its maximum

value $\eta_{max}^{\mathrm{dis}} = 3/2$ is obtained when the momentum relaxation is dominated by large angle scattering from short-range impurities.

Comparing the empirical fit to $\Delta\sigma/\sigma$, presented in Eq. (74) in Sec. 4.1 to Eq. (76), can relate the fitting parameters to the factors introduced by the microscopic models as follows

$$A_\epsilon = 2\pi\eta\mathcal{P}S_\pm, \tag{84}$$

$$\alpha = \frac{2\pi}{\omega\tau_q}. \tag{85}$$

The fact, that the damping coefficient α is smaller for both, larger τ_q and ω as well, explains why the observed oscillations are well resolved up to high ϵ, although the amplitude is reported to scale with ω^4 [14, 26]. It has to be addressed here, that the quantum lifetime τ_q extracted from $\alpha = 0.97$ for sample #A is smaller than the quantum lifetime extracted from the transport data for the identical sample by a factor of 3. A deviation of τ_q for those two methods is also reported in Ref. [26] and attributed to long-range potential fluctuations which lead to an additional damping of the SdH oscillations but have no influence on the MIRO amplitude [10].

In theory, the magnetic field enters the amplitude A_ϵ via the factor $\epsilon = \omega/\omega_c$ in Eq. (78). For small magnetic field values B, however, $\epsilon \gg 1$ and hence the amplitude becomes B-independent. It can be replaced by $A_\infty^{\mathrm{exp}} = A_\epsilon|_{\epsilon\to\infty}$. Note that together with the B-dependence also the polarization dependence vanishes for $\epsilon \gg 1$. Figure 18 shows, that the data collected for sample #A can be perfectly fitted by Eq. (78) for $\epsilon > 3$.

For Sample #A the amplitude A_∞ can be estimated using Eq. (84), which gives

$$A_\infty^{\mathrm{th}} = 2\pi\eta\mathcal{P}S_\infty \simeq \frac{(2\pi\hbar)^3 e^2 n_e^2 E_\omega^2}{m^3\tau_p T^2\omega^4}. \tag{86}$$

Here, for $\phi = -0.04$ and for $\Gamma = 0.19$ the polarization factor is $S_\infty = S_\pm|_{\omega\gg\omega_c} \lesssim 1$, i.e. there is almost no screening away from B_{CR}. From $B_{CR} = 1.84$, which

Sample	T(K)	B_{CR} (T)	$\delta\epsilon$	α	$10^3 \cdot A_\infty^{\exp}$	$10^3 \cdot A_\infty^{\text{th}}$	$\tilde{\phi}$
#A	4.2	1.84	-0.09	1	56	40	-0.04
#B	9.4	1.8	-0.09	0.6	1.3	1.7	-0.1
#C	15	1.8	0.09	2.6	-	5	0.15
#D	15	1.9	0.01	1.6	24	8	-0.07
#E	4.2	1.8	-0.05	1.2	20	9	-0.1

Table 2: The CR magnetic field position B_{CR}, the additional phase $\delta\epsilon$, the damping coefficient α, and the oscillation amplitude $A_\epsilon^{\exp}$ extracted from fitting of the photoconductivity oscillations after Eq. (74) and the measurement temperature T. $A_\epsilon^{\exp}$ for sample # C could not be reliably extracted, due to the small number of resolved oscillations. Added to that are the theoretically predicted amplitude A_ϵ^{th} and the interference parameter $\tilde{\phi}$. The amplitudes $A_\epsilon^{\exp}$ and A_ϵ^{th} are in good agreement.

is extracted from the period of the oscillations one obtains $m = 0.074 m_0$, and together with $T = 4.2\,\text{K}$ $\eta^{\text{in}} \simeq 12$ is identified. The displacement contribution $\eta^{\text{dis}} \leq 3/2 \ll 12$ can, hence, be neglected.

The estimated amplitude $A_\infty^{\text{th}} \simeq 0.04$ coincides with the empirical amplitude $A_\infty^{\exp} = 0.056$ very well. The data for the empirical and the estimated amplitudes, determined separately for every sample is presented in Tab. 2 together with the fractional part $\tilde{\phi}$ of ϕ.

4.3 Circularly Polarized Terahertz Radiation Induced Resistivity Oscillations

The previous section revealed, that the observed oscillations are well described by the inelastic mechanism. This mechanism is supposed to be strongly dependent on the helicity of circularly polarized radiation, see Sec. 2.2.4. In the following TIRO are probed with right- and left-handed circularly polarized radiation and the results are analyzed in accordance of the microscopic mechanisms presented in Sec. 2.2.4.

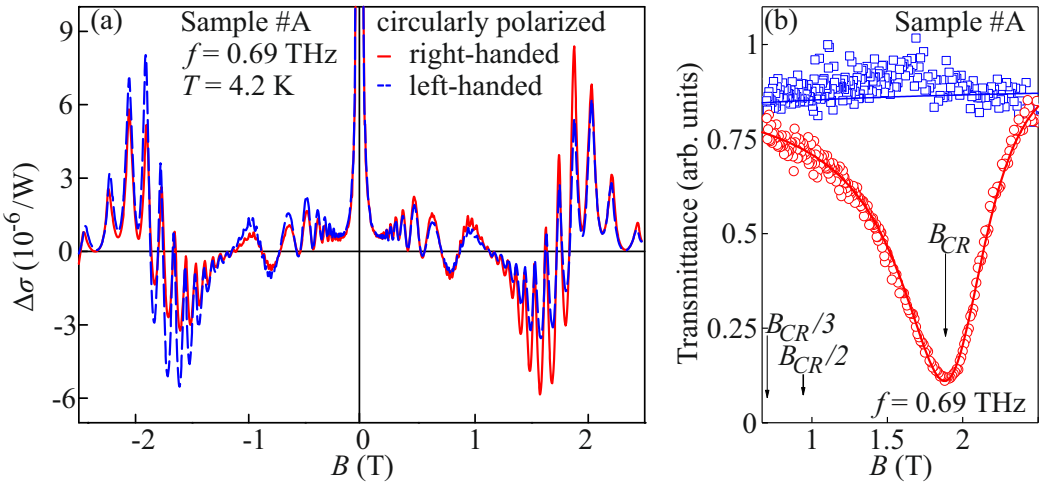

Figure 22: (a) Magneto-oscillations of the photoconductivity induced by circularly right- (red lines) and left-handed polarized radiation of the frequency $f = 0.6$ THz obtained at $T = 4.2$ K. Transmittance showing CR active behavior for circularly right-handed polarization (blue) and CR inactive behavior for left-handed polarization. The transmittance data is collected parallel to the photoconductivity and, hence also at $f = 0.69$ THz and $T = 4.2$ K.

4.3.1 Results

The influence of right- or left-handed circularly polarized radiation on the photoconductivity signal is shown in Fig. 22 (a), obtained at $T = 4.2\,\mathrm{K}$ and induced by radiation of the frequency $f = 0.69\,\mathrm{THz}$. The data, obtained for right-handed circular polarization is represented by the red solid line, the data for left-handed circular polarization is presented as blue dashed line. TIRO are observed for both polarizations and also both magnetic field directions, as well as traces of the SdH oscillations. For magnetic fields up to $B = |1|\,\mathrm{T}$ there's rarely any helicity dependence present, whereas the obtained data defers slightly for the two polarization states at fields between $B \approx |1|\,\mathrm{T}$ and $B \approx |2.5|\,\mathrm{T}$.

For the investigation of helicity dependent effects in this section, the photoconductivity data are supplemented by transmittance data which are recorded simultaneously. The additionally obtained transmittance data presented in Fig. 15 (a) in Sec. 4.1 is shown again in Fig. 22 (b) for easier comparison to the photoconductivity data. Since both, photoconductivity and transmission are

recorded during the same measurement, the experimental conditions are exactly the same for both results. Only transmittance data for positive magnetic field $B > 0$ are shown. The data for the CRI regime, for positive magnetic field induced by left-handed helicity, represented by blue squares is roughly constant over the whole range of the measurement, whereas for CRA, induced by right-handed polarization, marked by red circles, the transmittance signal drops down to nearly zero at $B = 1.88\,\mathrm{T}$. The magnetic field position B_{CR} of the CR and its higher harmonics are marked by vertical arrows in Fig. 22 (b). The red and blue solid lines represent fits, which is discussed in the following subsection. Data obtained from the fits are the basis of the approach to explain the weak helicity dependence.

4.3.2 Discussion

The presence of a strong sensitivity of the transmittance signal to the CR in Fig. 22 (b) shows, that the quality of circular polarization is very high at the 2DEG. The transmission data is well fitted by the transmission coefficient T, see Eq. (79), taking into account screening due to multiple surface reflexions and superradiant decay. There, the helicity comes in by the factor $\tilde{y}$.

The screening function $|s_{\pm}|^2$, which enters the description of TIRO in Eq. (76), also includes T. Therefore, TIRO are expected to depend strongly on the helicity in the range $\omega \sim \omega_c$. The observed helicity dependence of the photoconductivity signal, however, is much weaker. A closer look at Eqs. (79), (82), and (78) reveals, that the minimum ratio of the TIRO signal for CRA and CRI configurations is expected in the case of constructive interference, when

$$S_{\pm} = \frac{1}{(\Gamma+\gamma)^2 + (1 \pm \omega_c/\omega)},\ \cos^2\phi = 1. \tag{87}$$

If a positive magnetic field is taken into account and considering that $\gamma \ll \Gamma$ the ratio is given by

$$\frac{A_{\epsilon}^{\mathrm{CRA}}}{A_{\epsilon}^{\mathrm{CRI}}} = \frac{(1+\omega_c/\omega)^2 + \Gamma^2}{(1-\omega_c/\omega)^2 + \Gamma^2}. \tag{88}$$

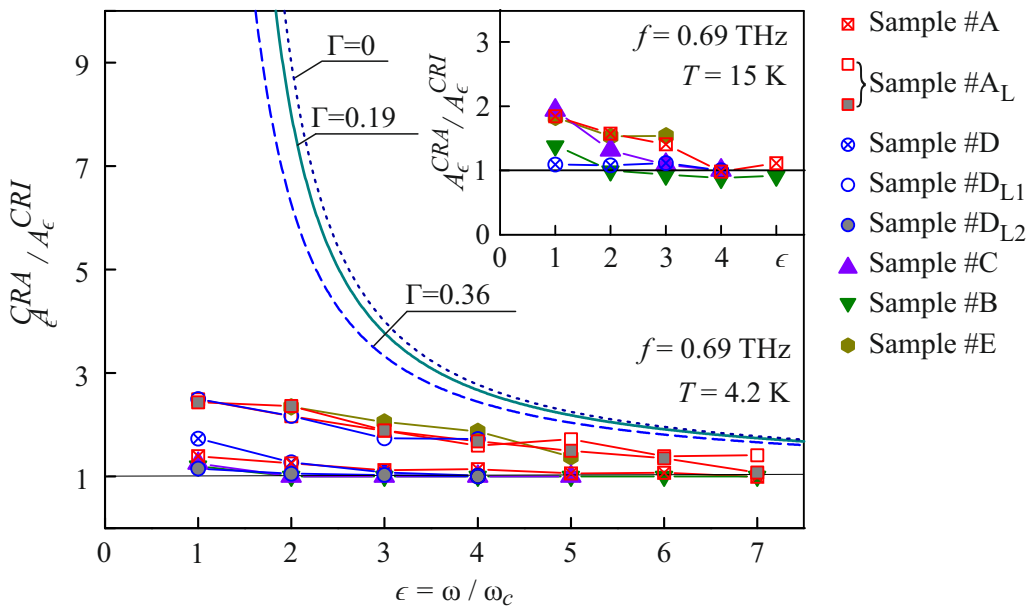

Figure 23: The ratio $A_\epsilon^{\mathrm{CRA}}/A_\epsilon^{\mathrm{CIA}}$ of the TIRO amplitude measured for CR active and inactive polarization in respect to ϵ for samples from five different wavers. The index L marks samples with large Corbino structures ($r_i = 0.25\,\mathrm{mm}$, $r_o = 4.25\,\mathrm{mm}$). Fits after Eq. (88) for $\Gamma = 0.19$ and $\Gamma = 0.36$, which are the respective values for samples #A and #D.

Though Γ reduces the difference between CRA and CRI, there's still a strong difference present between the predicted and measured ratio for CRA and CRI for all probed samples. This is shown in Fig. 23. Even for sample #D, which has the largest $n_e = 2.4 \times 10^12\ \mathrm{cm}^{-2}$ and hence, the largest $\Gamma \simeq 0.36$, the theoretical value at $\epsilon = 1, 2, 3$ is by far larger than observed in experiment. For lower densities n_e or for ϕ differing more from zero value, the ratio can only increase.

The inelastic and displacement mechanisms describe the experimental observed data well for high harmonics at $\omega \gg \omega_c$, for low harmonics, however the behavior can not be explained by any existing theory. A saturation effect can also be ruled out since the amplitudes of the absorbed oscillations scale linearly in intensity, as shown in Fig. 16. A more comprehensive analysis of the intensity dependence of TIRO is presented in the following section, applying a high power THz laser.

4.4 High Intensity Terahertz Radiation Induced Resistivity Oscillations

So far all presented results have been obtained by irradiation with intensities around $I = 110\,\mathrm{mW/cm^2}$. The only exception is the observation for $f = 1.62$, where due to the unsteady background only a qualitative analysis is possible. As previously shown in Sec. 4.1 MIRO amplitudes scale linearly with power in this range. For much higher intensities, however, very interesting physics is predicted to happen [10, 35]. Due to the lack of powerful sources in the microwave range, by now not much work is done in this field [29, 35]. The utilization of a high power line-tunable molecular THz laser pumped by a pulsed TEA CO_2 laser allows to reach intensities up to $I = 10^4\,\mathrm{W/cm^2}$, which is five orders of magnitude higher than the intensity achieved on the cw-system. Applying such high powers holds several benefits. Despite MIRO amplitudes being predicted to strongly decrease with growing frequency f, TIRO are obtained and analyzed by irradiation with frequencies up to $f = 1.07\,\mathrm{THz}$ in the following section. Moreover, TIRO are observed on samples cooled down and probed in complete darkness, although illumination with visible light was considered mandatory for the observation of MIRO to the day [14]. All data presented in this section are obtained at $T = 4.2\,\mathrm{K}$.

4.4.1 Results

The photoconductivity $\Delta\sigma$ in respect to the magnetic field B is presented in Fig. 24 (a) and (b) for the samples #B and #A, respectively. In Fig. 24 (a) $\Delta\sigma$ is induced by radiation of the frequency $f = 1.07\,\mathrm{THz}$ and the intensity $I = 70\,\mathrm{W/cm^2}$. Strong oscillations are observed in the region between $|B| \approx 0.3\,\mathrm{T}$ and $|B| \approx 3\,\mathrm{T}$, having the same amplitudes for both right- and left-handed circularly polarized radiation. Figure 24 (b) shows photoconductivity oscillations ranging form $|B| \approx 0.3\,\mathrm{T}$ to $|B| \approx 2\,\mathrm{T}$ induced by radiation of the frequency $f = 0.60\,\mathrm{THz}$, an intensity of $I = 0.6\,\mathrm{kW/cm^2}$, and right-handed circular polarization. Starting from $|B| \approx 1\,\mathrm{T}$ a second class of oscillations is observed in both samples.

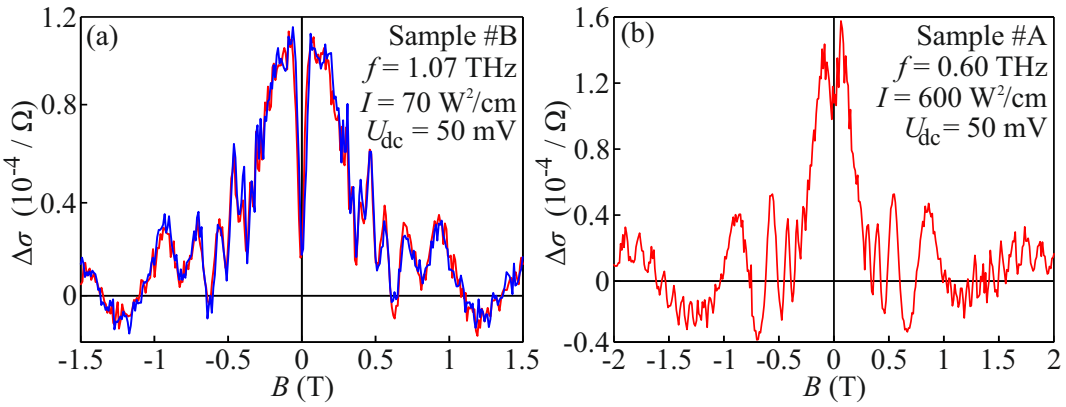

Figure 24: Photoconductivity $\Delta\sigma$ as a function of the magnetic field, induced by pulsed THz radiation. Panel (a) shows data of sample #B induced by radiation of the frequency $f = 1.07\,\mathrm{THz}$ and an intensity $I = 70\,\mathrm{W/cm^2}$. Red lines represent circularly right-handed and blue lines left-handed polarized radiation. Data for $f = 0.6\,\mathrm{THz}$ and $I = 600\,\mathrm{W/cm^2}$ is presented in panel (b).

As shown in Sec. 4.1, an analysis of the $1/B$-periodicity can be observed easily, when the photoconductivity data is presented as a function of ϵ, see Fig. 25. The normed photoconductivity $\Delta\sigma/\sigma$ measured on samples #B, #D, and #E, induced by high intensity radiation is shown in this figure. Strong oscillations are observed, whose extrema are found symmetrically offset around integer values of ϵ. All samples show a background, that is nearly B-independent and a decrease in oscillation amplitude with growing ϵ. A significant influence of the radiation's helicity couldn't be observed in either of the probed samples. The oscillations shown in Fig. 25 (a) are slightly different to the oscillations observed on the other samples. The 4th harmonic has a larger amplitude than usual and the 5th a smaller one, which is in line with the low-intensity observations and seems to be present only in this specific sample.

Especially beneficial for this work is the fact that, starting from a very high initial intensity, the sample can be irradiated by radiation over a large range of intensities by simply putting attenuators into the beam path. Figure 26 shows the normed photoconductivities $\Delta\sigma/\sigma$ as a function of ϵ for five different intensities, ranging from $I = 7\,\mathrm{W/cm^2}$ to $I = 2500\,\mathrm{W/cm^2}$. Despite this particular sample demonstrating a somewhat irregular shape of MIRO, this

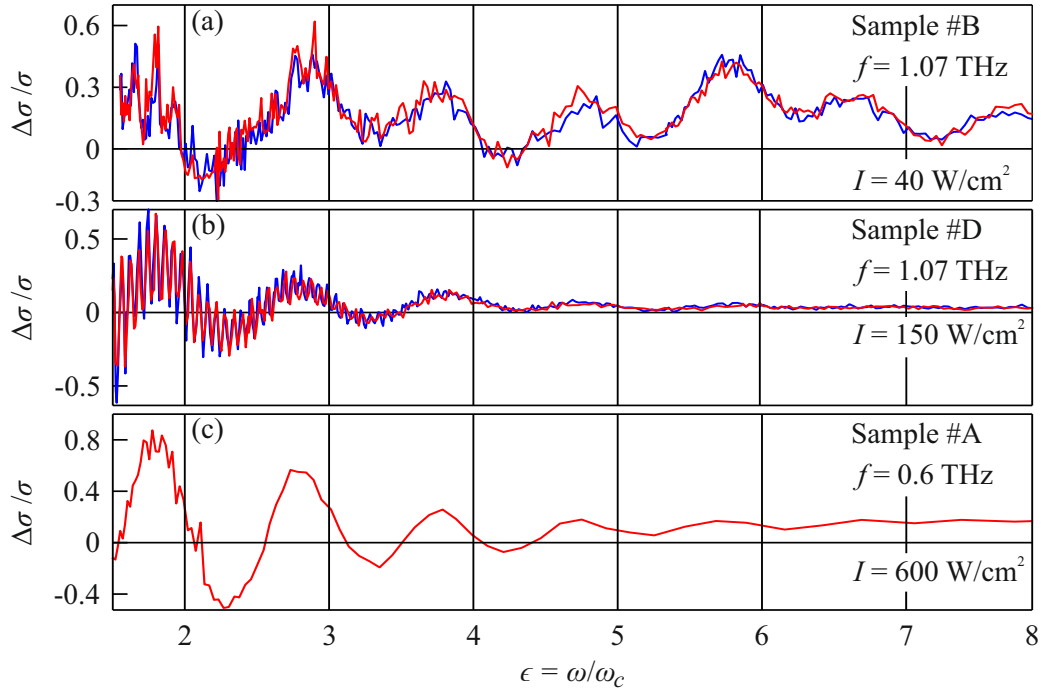

Figure 25: Photoconductivity $\Delta\sigma$ normed to dark conductivity σ as a function of ϵ, induced by pulsed THz radiation. Red lines represent circularly right-handed and blue lines left-handed polarized radiation. Panel (a) shows data of sample #D induced by radiation of the frequency $f = 1.07\,\mathrm{THz}$ and an intensity $I = 40\,\mathrm{W/cm^2}$. Data for $f = 1.07\,\mathrm{THz}$ and $I = 150\,\mathrm{W/cm^2}$ is presented in panel (b). Panel (c) shows $\Delta\sigma/\sigma$ obtained in sample #A for $f = 0.6\,\mathrm{THz}$ and $I = 600\,\mathrm{W/cm^2}$.

shape is well reproduced for all intensities. The position of the minima and maxima as well as the relative magnitude of all features is preserved and only the amplitude is sensitive to radiation power. A comprehensive analysis of the intensity dependence is given in the following subsection.

In order to probe the Corbino geometry's influence that is discussed in Sec. 3, the photoconductivity of three samples from the same waver, but with different inner Corbino radii r_i, has been measured. The outer Corbino radius is the same for all three samples. Figure 27 (a) shows the detected voltage drop on the load resistor for the three samples. The signals are bigger for larger r_i. The photoconductivity, presented in Fig. 27 (b), however takes into account the geometrical factor for Corbino disc samples $1/(2\pi)\ln(r_o/r_i)$ shows almost the

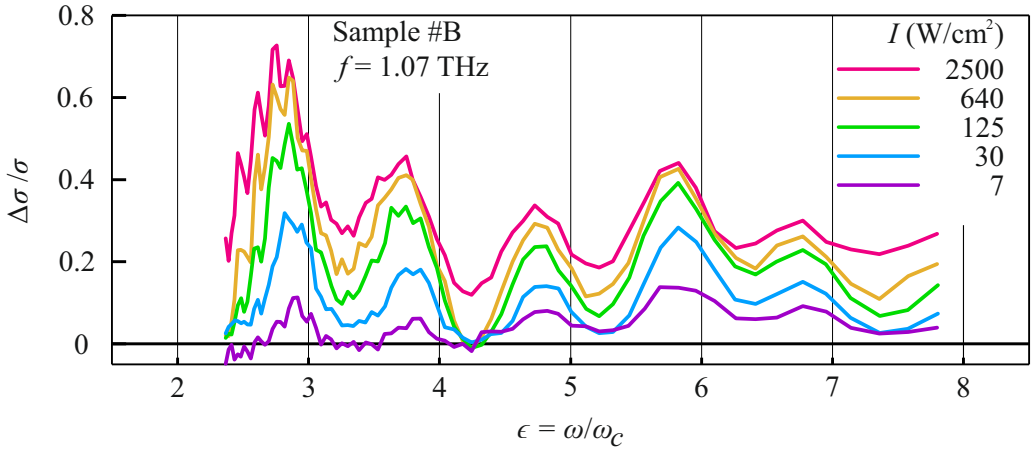

Figure 26: Normalized photoconductivity $\Delta\sigma/\sigma$ as a function of ϵ for sample #B induced by radiation with the frequency $f = 1.07\,\mathrm{THz}$ for five different intensities varying between $I = 7\,\mathrm{W/cm^2}$ and $I = 2500\,\mathrm{W/cm^2}$, color coded according to the legend.

same dependence for all three samples. Only for the sample with the largest $r_i = 2.5\,\mathrm{mm}$ the signals are a bit smaller. This can be attributed to a decrease of incident radiation intensity, which is analyzed in detail in Sec. 4.2. The intensity reduction in this case originates from the larger area of the sample which is covered by the non-transparent gold film of the central contact.

In Sec. 4.2 it is demonstrated, that for intensities in the range of $I \approx 110\,\mathrm{mW/cm^2}$ TIRO originate from the bulk. In the case that bulk- and boundary conditions are present at the same time, but dominated for low I, one can expect that the bulk effects saturate earlier and hence, a strong edge or contact effect is observed at high I. The illumination of the sample edges with high power THz radiation, is presented in Fig. 28. The red dots in Fig. 28 (b) represent the oscillation amplitude $\Delta_3\sigma_{norm}$ for the third harmonic, $\epsilon = 3$, extracted from photoconductivity measurements at the positions of the laser on the sample, indicated on the abscissa of the figure normed to the maximum value of the oscillation amplitude $\Delta_3\sigma_{max}$. In which way x is defined by the laser spot position in relation to the sample is illustrated by the scheme in Fig. 28 (a). The red line represents the calculated power of the laser spot passing the gold Corbino contact areas of the samples used in this work. For this calculation

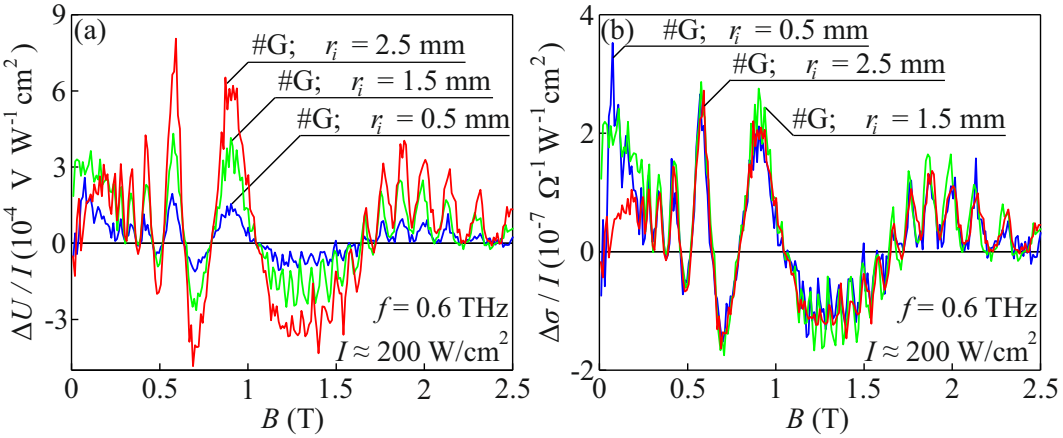

Figure 27: Photo induced voltage drop signal ΔU (a) and the photoconductivity $\Delta\sigma$ (b) as a function of B, both normalized to the radiation intensity I. Samples are processed with different inner Corbino radii $r_i = 0.5\,\text{mm}$, $r_i = 1.5\,\text{mm}$, and $r_i = 2.5\,\text{mm}$, represented by blue, green, and red lines, respectively. The outer Corbino radius $r_o = 4.25\,\text{mm}$ is identical for all three samples.

the laser beam profile is assumed to be perfectly Gaussian with a full width at half maximum of 40 mm, which is realistic, compared to the experimental parameters presented in Sec. 3. The data follow the calculated intensity very well. This observation confirms that also for very high intensities the boundaries do not contribute to the generation of TIRO.

Previous works on MIRO are carried out in most cases at very low temperatures $T < 4.2\,\text{K}$ and after illumination with visible light. The second requirement is considered to be mandatory in order to obtain sufficiently high carrier densities $n_e \sim 10^{11}\,\text{cm}^{-}2$ together with high enough mobilities $\mu \geq 10^6\,\text{cm}^2/\text{Vs}$ to observe MIRO [14]. In Fig. 29 (a) the photoconductivity $\Delta\sigma$ in respect to the magnetic field B is shown for two experimental conditions: the blue line represents the photoconductivity signal induced into sample #B that is cooled down in a cryostat with windows, which are closed with a black PE sheet, absorbing the visible light but transmitting the THz radiation. Before the measurement, however, the sheet is removed to illuminate the sample with visible light. The orange line, in contrast, is measured on the same sample, but without any illumination by visible light. Whereas for the illuminated sample pronounced TIRO are observed, for the sample in the dark only weak traces of oscillations at

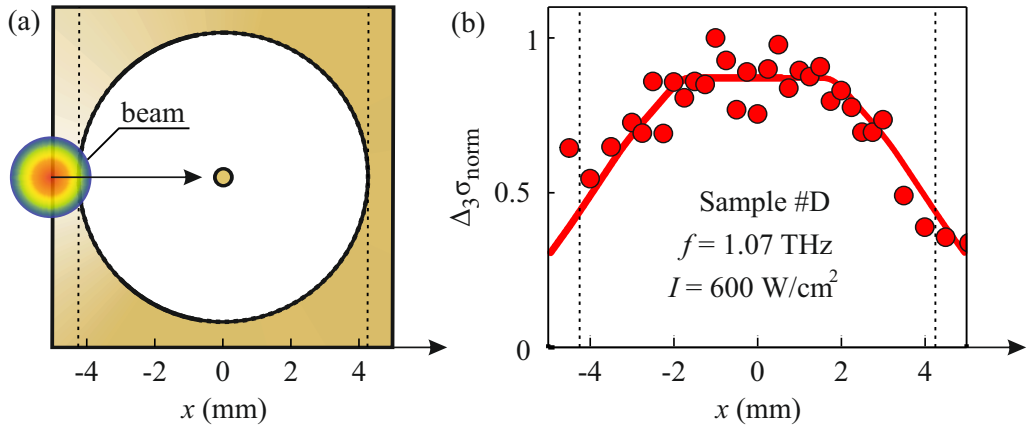

Figure 28: (a) Sketch of the laser spot scanning over the Corbino disc sample. (b) Normed photoconductivity amplitude $\Delta_3\sigma_{norm}$ as a function the laser spot position on the sample, represented by the red dots. The red line represents the calculated power which is irradiated on the 2DEG, taking into account the reflection at the AuGe contacts of the sample.

low ϵ are present. Considering the complete absence of MIRO in the microwave range under these conditions, however, the observation of even these small traces is already surprising. The photoconductivity data is supplemented by the results of magnetotransport measurements for both experimental conditions. While the general slope is quite similar for both, indicating that the mobility μ of the sample does not change much, the positions of SdH-oscillation extrema shift, indicating a rise of carrier density n_e induced by visible light.

4.4.2 Discussion

Datasets for three different samples irradiated by high intensity THz radiation are presented in Fig. 24. In all of them, two types of oscillations occur. Comparison to the magnetotransport data allows to attribute the oscillations at higher magnetic field to the traces of SdH oscillations, which appear due to electron gas heating, see Sec. 2.2.2. The second oscillation type reminds one on the MIRO-like oscillations analyzed for lower intensity cw radiation in the previous sections. Their ϵ-periodic nature becomes clear in Fig. 25, as well as the strong damping for higher ϵ. A closer look at Fig. 24 also reveals that, due

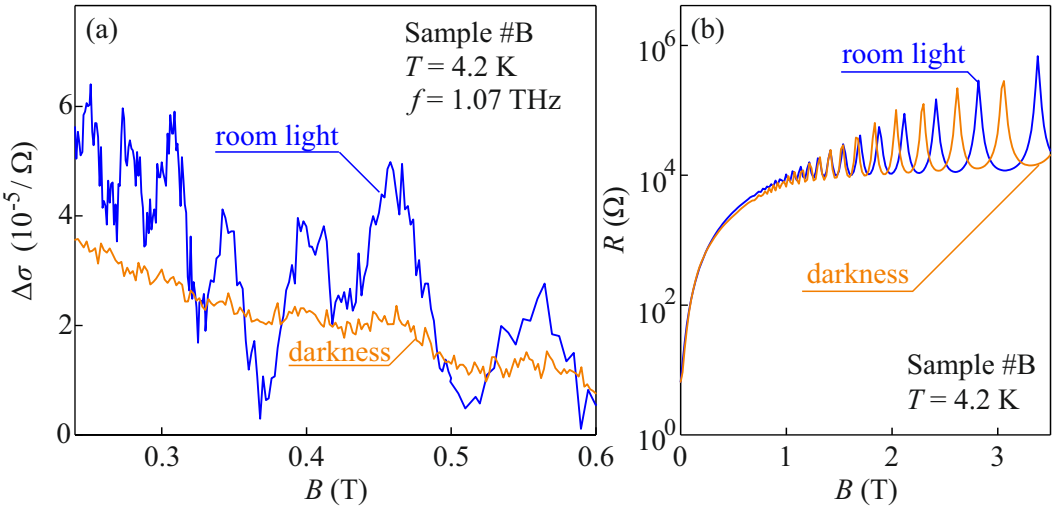

Figure 29: (a) Photoconductivity $\Delta\sigma$ as a function of magnetic field strength B induced by radiation with $f = 1.07\,\mathrm{THz}$ at $T = 4.2\,\mathrm{K}$. The data represented by the blue line is obtained while the sample is illuminated by room light. The orange line represents data, for which the sample is cooled down and probed without any illumination with visible light. Panel (b) shows magnetotransport data obtained under the same conditions, except for THz irradiation. The color coding is identical to panel (a).

to $\epsilon = \omega/\omega_c$, the oscillations positions are at higher B for higher frequencies. The helicity dependence for all probed samples is even less pronounced than for the low power excitation data. In fact, it is completely hidden by the noise in the high intensity data, which is larger in the pulsed regime, since here each pulse has its individual, sub-nanosecond intensity structure, which yields a strong deviation of maximum intensity for every single pulse. Though each single pulse's intensity is corrected by the intensity obtained from a reference detector, the deviation can not be completely compensated. The absence of a helicity dependence at high intensities, however, is not as surprising, since one would expect possible saturation effects to suppress the helicity dependence also in the case of a more pronounced helicity dependent photo-response at low I.

The oscillation amplitude A_ϵ and the damping parameter α can be taken from the data shown in Fig. 25, similarly to the procedure in Sec. 4.1 by fitting with

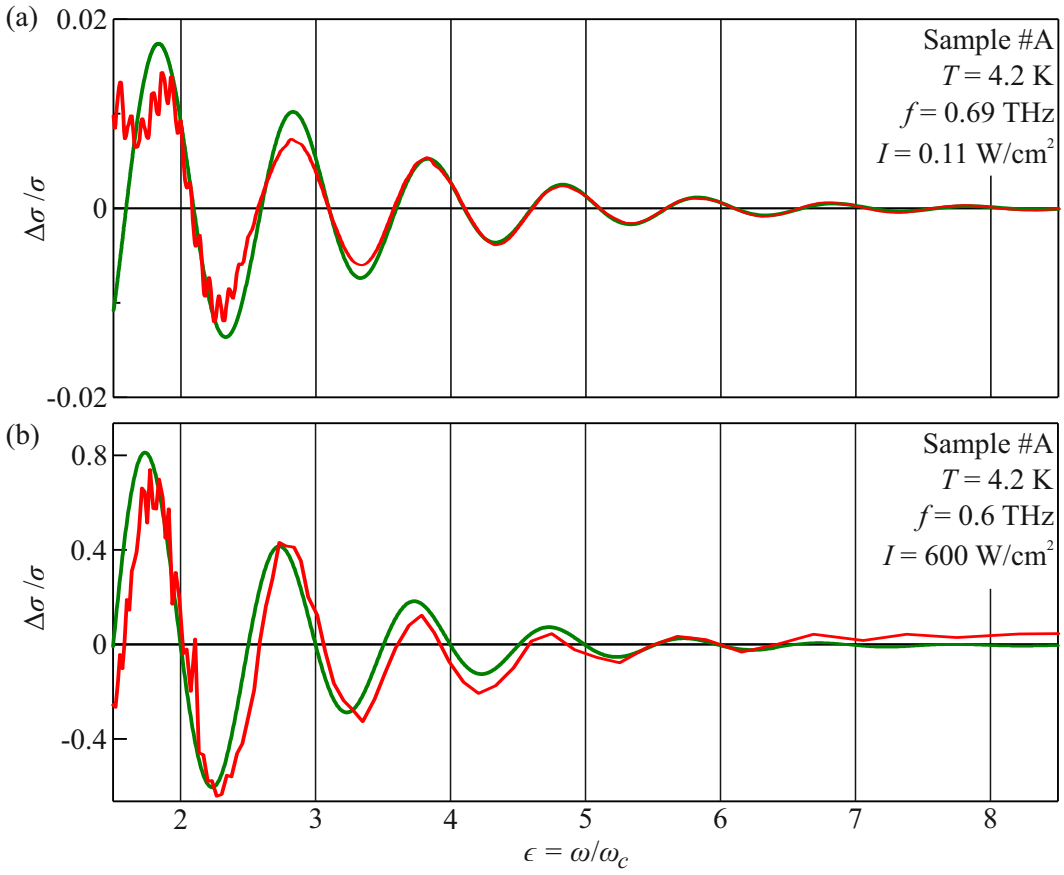

Figure 30: Normed photoconductivity $\Delta\sigma/\sigma$ data (red lines) and fits (green lines) after Eq. (74) in respect to ϵ for sample #A at $T = 4.2$ K. The data are induced by radiation of the frequency $f = 0.69$ THz and the intensity $I = 0.11$ W/cm^2 in panel (a), and $f = 0.6$ THz and $I = 600$ W/cm^2 in panel (b).

Eq. (74). Figure 30 (a) and (b) allows to compare directly the ϵ-dependent normed photoconductivity $\Delta\sigma/\sigma$ of sample #A for cw-excitation in (a) with $f = 0.69$ THz and $I = 0.11$ W/cm^2 , to the one exited by pulsed radiation with $f = 0.6$ THz and $I = 600$ W/cm^2 in panel (b). The red lines here represent the measured data, whereas the green ones represent the fit according to Eq. (74). Note that the constant background is removed for easier fitting. The fits give the exactly identical values for the damping parameter α in both cases, leaving no doubt that the observed effects for both excitation intensities are MIRO. Note that also the phase $\varphi = \pm 1/4$, which describes the positions of MIRO

minima (+) and maxima (-) is conserved up to $I = 600$ W/cm^2. This is insofar surprising, as there are reports on a reduced phase for high intensities in the microwave range [29, 42, 68]. Also the additional oscillating features reported earlier for high I microwave excitation [21, 35, 69–74] are not present in the THz induced photoconductivity. Both features are also absent in the photoconductivity in respect to ϵ which is presented for different intensities up to $I = 2.5\,\mathrm{kW/cm^2}$ in Fig. 26. The only factor in both figures, that depends on I is the oscillation amplitude. However for the highest intensities applied, $I \geq 125\,\mathrm{W/cm^2}$, the amplitude does not grow as strongly as for lower I. The differences between the high-power THz and microwave responses suggest distinct mechanisms of the nonlinearity.

A detailed analysis of the intensity dependence of the oscillation amplitude can be achieved by separating $\Delta\sigma/\sigma$ into two contributions $\Delta\sigma = \Delta\sigma_{osc} + \Delta\sigma_{bg}$ with $\Delta\sigma_{osc}$ being the oscillatory and $\Delta\sigma_{bg}$ being the nearly B-independent part.

To analyze the amplitude's intensity dependence in more detail the difference between maximum and minimum values of $\Delta\sigma_{osc}$ around a node at $\epsilon = N$ is extracted. It is denoted as the amplitude $\Delta_N\sigma$ at this certain position. In Fig. 31 (a) $\Delta_3\sigma$ is presented in respect to the radiation's intensity I. The data, represented by the black dots show, that the oscillation amplitude grows linearly at low intensities and saturates at high ones. The dashed line represents a linear fit, $\Delta_3\sigma \propto I$, whereas the solid line corresponds to a saturation of $\Delta_3\sigma$. To quantify this saturation behavior the intensity range of the analysis is extended in Fig. 31 (b) by presenting the data on a double-logarithmic scale. The normalization of the photoconductivity $\Delta\sigma$ to the intensity I allows to easily compare MIRO magnitudes for different radiation frequencies. In Fig. 31 (b) the reduced amplitude $\Delta_3\sigma/I$ induced to sample #B by radiation with three different frequencies is presented. The solid lines represent the fits following the empirical equation

$$\Delta_N\sigma/I = \frac{1}{(1 + I/I_S)^\beta}, \tag{89}$$

describing the saturation of the reduced amplitudes. The fitting parameter $\beta \approx 1.3$ is very similar for all three frequencies while the saturation intensity I_S grows

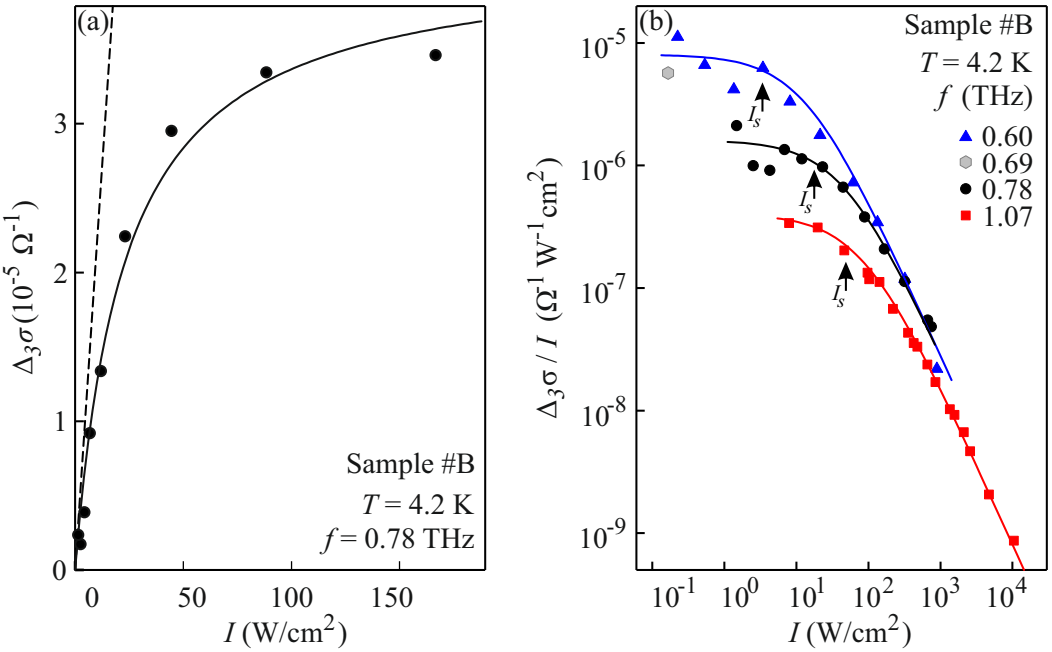

Figure 31: (a) Intensity dependence of the oscillation amplitude $\Delta_3\sigma$ at the oscillation order $\epsilon = 3$ for sample #B. The data is presented in a linear-linear plot. The solid line corresponds to a fit using $\Delta_3\sigma \propto I/(1 + I/I_s)^{1.3}$ and the dashed line corresponds to a linear fit $\Delta_3\sigma \propto I$. (b) Intensity dependence of the reduced oscillation amplitude $\Delta_3\sigma/I$. The hexagon presents the result obtained using low power cw laser operating at $f = 0.69$ THz, see Sec. 4.1. Other data points correspond to excitation by THz laser pulses at three different frequencies. Solid lines are fits using $\Delta_3\sigma/I \propto (1 + I/I_s)^{-1.3}$. Saturation intensities used for the fits are indicated by arrows and are given by $I_s = 15$ W/cm^2 ($f = 0.6$ THz), $I_s = 45$ W/cm^2 ($f = 0.78$ THz), and $I_s = 85$ W/cm^2 ($f = 1.07$ THz).

with the radiation frequency. In the linear regime a strong frequency dependence is present, but as the intensity increases the saturated photo-response becomes virtually frequency independent. For comparison, an additional data point is shown, representing the amplitude extracted from the low power cw laser experiments at $f = 0.69$ THz presented in Fig. 31 (a), corresponding well to the high intensity data.

The intensity dependence described by Eq. (89) also holds for different samples, e. g. shown for sample #A in Fig. 32 (b). However, the saturation intensity

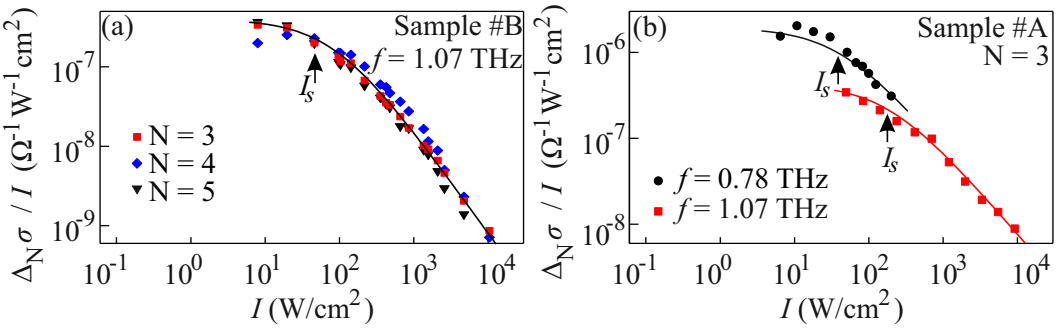

Figure 32: Intensity dependence of the oscillation amplitude normed to the intensity $\Delta_N\sigma/I$. Solid lines are fits using $\Delta_3\sigma/I \propto (1 + I/I_s)^{-\beta}$. Panel (a) shows $\Delta_N\sigma/I$ for different oscillation orders, N =3, 4, and 5, measured on sample #B under illumination with $f = 1.07$ THz. The solid line is the fit using $\beta = 1.3$ and $I_s = 85$ W/cm^2. Panel (b) presents $\Delta_3\sigma/I$ measured on sample #A under $f = 0.78$ and 1.07 THz radiation. The solid lines are fits using $\beta = 1$ and saturation intensities $I_s = 30$ (190) W/cm^2 for $f = 0.78$ (1.07) THz.

I_S for sample #A is several times larger than for sample #B. The description is furthermore valid for all ϵ, see Fig. 32 (a), where $\Delta_N\sigma$ of sample #B is presented for $N = 3, 4, 5$. Actually, the same fitting parameters, including I_S can be applied to the data for all ϵ of sample #B.

As addressed above, the background can be extracted as a nearly smooth line, which connects the oscillation's nodes at integer ϵ in the normed photoconductivity $\Delta\sigma/\sigma$. The background photoconductivity $\Delta_{\rm bg}/I$ normed to the intensity I, extracted in the vicinity of $\epsilon = 3$, corresponding to $B = B_{CR}/3$ is shown in Fig. 33. The background is also sublinear. However, the nonlinearity sets in at lower I, compared to TIRO. At high intensities $\Delta\sigma_{\rm bg}$ scales proportional to I^ζ with $0 \leq \zeta \leq 0.2$.

In the following, an analysis of the intensity dependence presented in the Figs. 31 and 32 is given, concluding that in the THz range the major source of saturation in an irradiated sample is electron gas heating. One of the main reasons for this is, that the absorption of radiation responsible for heating is proportional to the inverse square of the radiation frequency f^{-2}, while the MIRO amplitude scales as f^{-4}, see e.g. Ref. [10]. The value of the amplitude A_ϵ is modulated by the higher electron temperature $T_e(I)$ in this case. The phase and shape, however,

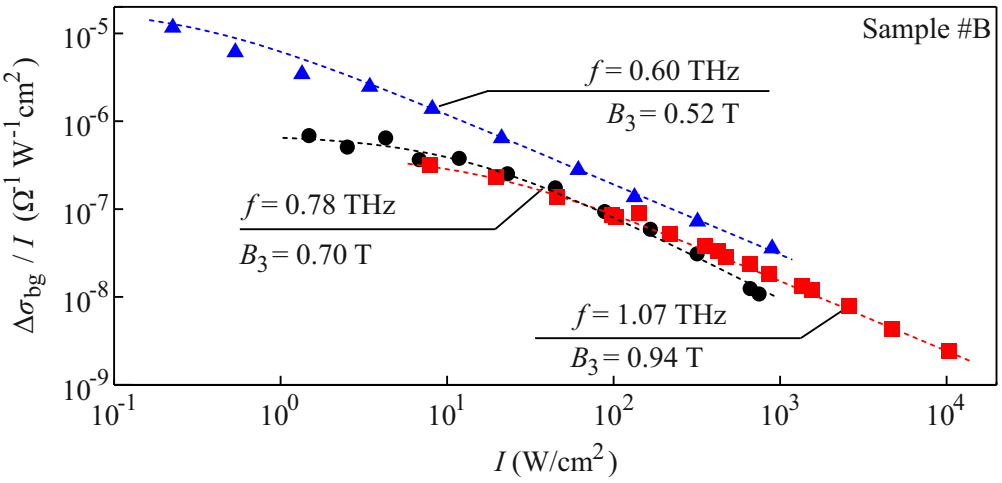

Figure 33: The background part $\Delta\sigma_{\rm bg}$ of the photoconductivity normalized to the radiation intensity I measured on sample #B for three radiation frequencies. Dashed lines are guide for the eye.

are unaffected since $\sin(2\pi\epsilon)$ contains no quantities which are sensitive to T_e. The estimates below, using both microscopic models of MIRO and the results of low-intensity THz illumination from Sec. 4.1, support the heating approach. They show that the nonlinearities found in the microwave range would require much higher intensities in the THz range, and may even become out of reach in the presence of strong heating. Within the nonlinearity mechanism based on heating, not only the amplitude $A(I)$ but also the low-B damping parameter α can have an implicit intensity dependence through $T_e(I)$. Such a nonlinearity in α was identified before in the microwave range and was attributed there to the thermal broadening of Landau levels [29]. Here, however, the parameter α in the empirical expression in Eq. (74) does not depend on the intensity, see also Fig. 30. It agrees well with the values $\alpha = 1/\omega\tau_q \sim 1$ extracted for low intensities in Sec. 4.3.2.

In order to show that the thermal broadening of Landau levels is indeed negligible in the presented observations, the rate of inelastic electron-electron collisions, $\tau_{\rm in} \simeq \hbar\varepsilon_F/T_e^2$, where ε_F is the Fermi energy, has to be estimated. This gives $\tau_{\rm in} \sim 0.2$ ns for sample #A and $\tau_{\rm in} \sim 0.15$ ns for sample #B at $T_e = T_0 \equiv 4.2$ K. The associated high-power correction to α can be estimated [46, 62] as

$$\alpha(I) - \alpha(0) = 1/\omega\tau_{\rm in}(T_e) - 1/\omega\tau_{\rm in}(T_0) = \tilde{a}(T_e^2/T_0^2 - 1), \tag{90}$$

whith $\tilde{a} = 1/\omega\tau_{\rm in}(T_e = T_0)$. Since the resulting $\tilde{a} \lesssim 10^{-2}$ at $f = 1.07$ THz is relatively small ($\tilde{a} \simeq 4.7 \times 10^{-3}$ and for sample #A and $\tilde{a} \simeq 6.2 \times 10^{-3}$ sample #B) it is no longer surprising that no changes in α at the applied intensity is detected. Note that, according to the above estimation, the heating effect on α would become noticeable at higher intensities, for temperatures reaching values $T_e \gtrsim 10\, T_0$. This suggests that, despite the wide intensity range in the nonlinear regime of the presented experiments, this temperature is still not reached here. The observed situation is feasible, since heating is usually strongly nonlinear. In order to be compatible with the observed $\alpha \simeq \text{const}(I) \sim 1$ and the estimated $\tilde{a} \sim 10^{-2}$ above, the electron temperature should grow as $T_e \propto \sqrt{I}$ or slower in the nonlinear regime of heating.

Analysis of the data above shows that the intensity dependence of the amplitude of MIRO is well described by $A(I) \simeq cI(1+I/I_s)^{-\beta}$ with $\beta \sim 1$. In the previous experiments, see Sec. 4.3, corresponding to $I \ll I_s$ and thus, to $A(I) = cI$, a good agreement is found between the measured values of the amplitude A and its estimates obtained within inelastic mechanism [41, 46]. Under the assumption, that the inelastic mechanism also governs the nonlinear response, it can be figured out whether the observed intensity dependence is compatible with the temperature dependence of the parameters entering the theory. This theory predicts $A \propto I\tau_{\rm in}(T_e)\tau_p^{-2}$. Here τ_p^{-1} is the momentum relaxation rate and $\tau_{\rm in}^{-1}$, as addressed above, describes the thermalization rate which balances the changes in the energy distribution of electrons induced by radiation of the intensity I. Taking τ_p to be T_e-independent, the saturation of $A(I) \propto I/T_e^2$ at $I \gg I_s$ requires $T_e \propto I^{\beta/2} \sim \sqrt{I}$ in this regime. While generally, the sublinear dependence of the electron temperature on radiation intensity is well established for low-dimensional semiconductor systems at low temperatures [55, 75–79], the feasibility of the particular dependence $T_e \propto \sqrt{I}$ requires additional study which is out of scope of this thesis.

It has to be noted, that generally, it can not be excluded that the momentum relaxation rate τ_p^{-1} also becomes I-dependent at high intensities. For instance,

this could be due to non-equilibrium phonon effects. An inclusion of such effects into the theory is not straightforward, in particular if typical phonon energies become comparable to ω_c. On a qualitative level, however, it is reasonable to expect that the non-elasticity of scattering processes may only reduce the amplitude of non-equilibrium oscillations in the distribution function responsible for MIRO. Furthermore, τ_p may only decrease with the increase of I which would lead to an increase of A. Assuming $\tau_p \propto I^{-\eta}$ with $\eta > 0$ at highest I, one obtains from $A(I) \sim \text{const}(I)$, that $T_e \propto I^{1/2-\eta}$, which results in a slower increase of heating at high intensities.

5 Conclusion

This thesis reports on the observation and analysis of MIRO induced by THz laser radiation in GaAs heterostructures. By selective excitation of the bulk and boundaries of the GaAs 2DEG samples, the study demonstrates that MIRO are caused in the bulk for all applied frequencies in the THz range [66]. The oscillations are analyzed in the framework of the inelastic and the displacement mechanism [10, 46]. It is shown furthermore, that the dependence of the oscillations' magnitude on the polarization's helicity is weaker than theoretically expected [66]. Lastly, the work demonstrates that MIRO are very robust even for illumination with high power radiation. The intensity dependence of the oscillations' amplitude is intensively studied, revealing that electron gas heating is the dominant mechanism causing saturation in this frequency range [80].

THz photoconductivity experiments presented in this thesis show pronounced oscillations, induced by different THz frequencies. The oscillations are robust for frequencies up to 1.62 THz and temperatures up to 15 K. They are clearly identified to be MIRO. Additionally, it is demonstrated that by application of THz illumination, MIRO are observed on samples with mobilities much lower, than in samples for any reported observation of MIRO in the microwave range, see Sec. 4.1. Selective excitation of the sample's boundaries and the irradiation of solely the bulk by applying an aperture on top of the sample, as presented in Sec. 4.2, demonstrates that the oscillations originate from the whole bulk and not only the edges of the 2DEG. Consequently, the inelastic and the displacement mechanism [10, 46] are used to analyze the observed oscillations. In this thesis MIRO, excited by circularly right- and left-handed polarized radiation are also observed and studied in Sec. 4.3. The observed behavior can be described well by the inelastic and displacement mechanism for high harmonics, however the polarization dependence for low harmonics can not be explained by any existing theory. In Sec. 4.4, high radiation intensities in the kW range are applied to the 2DEG. The observed photoconductivity data reveal, that the oscillations preserve their properties even at high intensity irradiation. However, a saturation of the oscillation amplitude at high intensities is observed. By

analyzing the data, it is demonstrated that saturation is attributed to electron gas heating.

To conclude, the study allowed to answer some of the most intriguing, open questions in the field of MIRO. Furthermore, they enable further research on the topic. For instance, it is demonstrated, that MIRO can be studied on lower mobility samples if irradiated by THz radiation instead of microwaves. This helps to investigated MIRO on new material systems. Lately this has already been reported on HgTe quantum wells [81]. Concerning the polarization dependence of MIRO, experiments with varying linear polarization can provide new insights to the underlying mechanisms, especially if those experiments are performed for several temperatures. This could allow to separately observe oscillations that are dominated by either the displacement or the inelastic mechanism. To distinguish between the two mechanisms, also samples could be produced whose material properties selectively enhance one of the effects.

References

[1] Z. I. Alferov. "Nobel Lecture: The double heterostructure concept and its applications in physics, electronics, and technology". *Rev. Mod. Phys.* **73** (2001), 767–782.

[2] H. Kroemer. "Nobel Lecture: Quasielectric fields and band offsets: teaching electrons new tricks". *Rev. Mod. Phys.* **73** (2001), 783–793.

[3] T. Ando, A. B. Fowler, and F. Stern. "Electronic properties of two-dimensional systems". *Rev. Mod. Phys.* **54** (1982), 437–672.

[4] K. v. Klitzing, G. Dorda, and M. Pepper. "New Method for High-Accuracy Determination of the Fine-Structure Constant Based on Quantized Hall Resistance". *Phys. Rev. Lett.* **45** (1980), 494–497.

[5] R. B. Laughlin. "Nobel Lecture: Fractional quantization". *Rev. Mod. Phys.* **71** (1999), 863–874.

[6] H. L. Stormer. "Nobel Lecture: The fractional quantum Hall effect". *Rev. Mod. Phys.* **71** (1999), 875–889.

[7] D. C. Tsui. "Nobel Lecture: Interplay of disorder and interaction in two-dimensional electron gas in intense magnetic fields". *Rev. Mod. Phys.* **71** (1999), 891–895.

[8] D. Weiss et al. "Magnetoresistance Oscillations in a Two-Dimensional Electron Gas Induced by a Submicrometer Periodic Potential". *Europhys. Lett.* **8** (1989), 179–184s.

[9] D. Weiss et al. "Electron pinball and commensurate orbits in a periodic array of scatterers". *Phys. Rev. Lett.* **66** (1991), 2790–2793.

[10] I. A. Dmitriev et al. "Nonequilibrium phenomena in high Landau levels". *Rev. Mod. Phys.* **84** (2012), 1709–1763.

[11] C. L. Yang et al. "Zener Tunneling Between Landau Orbits in a High-Mobility Two-Dimensional Electron Gas". *Phys. Rev. Lett.* **89** (2002), 076801.

[12] M. A. Zudov et al. "New Class of Magnetoresistance Oscillations: Interaction of a Two-Dimensional Electron Gas with Leaky Interface Phonons". *Phys. Rev. Lett.* **86** (2001), 3614–3617.

[13] W. Zhang et al. "Resonant Phonon Scattering in Quantum Hall Systems Driven by dc Electric Fields". *Phys. Rev. Lett.* **100** (2008), 036805.

[14] M. A. Zudov et al. "Shubnikov–de Haas-like oscillations in millimeterwave photoconductivity in a high-mobility two-dimensional electron gas". *Phys. Rev. B* **64** (2001), 201311.

[15] R. G. Mani et al. "Zero-resistance states induced by electromagnetic-wave excitation in GaAs/AlGaAs heterostructures". *Nature* **420** (2002), 646.

[16] C. L. Yang et al. "Observation of Microwave-Induced Zero-Conductance State in Corbino Rings of a Two-Dimensional Electron System". *Phys. Rev. Lett.* **91** (2003), 096803.

[17] R. G. Mani. "Radiation-induced zero-resistance states with resolved Landau levels". *Appl. Phys. Lett.* **85** (2004), 4962–4964.

[18] R. G. Mani. "Radiation-induced oscillatory magnetoresistance in a tilted magnetic field in GaAs/Al_xGa_{1-x}As devices". *Phys. Rev. B* **72** (2005), 075327.

[19] R. Mani. "Photo-excited zero-resistance states in quasi-two-dimensional GaAs/Al_xGa_{1-x}As devices". *Solid State Commun.* **144** (2007). Spontaneous coherence in exciton systems, 409–412.

[20] M. A. Zudov et al. "Evidence for a New Dissipationless Effect in 2D Electronic Transport". *Phys. Rev. Lett.* **90** (2003), 046807.

[21] M. A. Zudov. "Period and phase of microwave-induced resistance oscillations and zero-resistance states in two-dimensional electron systems". *Phys. Rev. B* **69** (2004), 041304.

[22] M. A. Zudov et al. "Observation of microwave-induced resistance oscillations in a high-mobility two-dimensional hole gas in a strained Ge/SiGe quantum well". *Phys. Rev. B* **89** (2014), 125401.

[23] J. H. Smet et al. "Circular-Polarization-Dependent Study of the Microwave Photoconductivity in a Two-Dimensional Electron System". *Phys. Rev. Lett.* **95** (2005), 116804.

[24] S. Studenikin et al. "Microwave radiation induced magneto-oscillations in the longitudinal and transverse resistance of a two-dimensional electron gas". *Solid State Commun.* **129** (2004), 341–345.

[25] S. A. Studenikin et al. "Microwave-induced resistance oscillations on a high-mobility two-dimensional electron gas: Exact waveform, absorption/reflection and temperature damping". *Phys. Rev. B* **71** (2005), 245313.

[26] S. A. Studenikin et al. "Frequency quenching of microwave-induced resistance oscillations in a high-mobility two-dimensional electron gas". *Phys. Rev. B* **76** (2007), 165321.

[27] A. T. Hatke et al. "Microwave Photoresistance in dc-Driven 2D Systems at Cyclotron Resonance Subharmonics". *Phys. Rev. Lett.* **101** (2008), 246811.

[28] A. T. Hatke et al. "Temperature Dependence of Microwave Photoresistance in 2D Electron Systems". *Phys. Rev. Lett.* **102** (2009), 066804.

[29] A. T. Hatke et al. "Multiphoton microwave photoresistance in a high-mobility two-dimensional electron gas". *Phys. Rev. B* **84** (2011), 241302.

[30] A. T. Hatke et al. "Giant microwave photoresistivity in high-mobility quantum Hall systems". *Phys. Rev. B* **83** (2011), 121301.

[31] P. D. Ye et al. "Giant microwave photoresistance of two-dimensional electron gas". *Appl. Phys. Lett.* **79** (2001), 2193–2195.

[32] T. Ye et al. "Comparative study of microwave radiation-induced magnetoresistive oscillations induced by circularly- and linearly- polarized photo-excitation". *Sci. Rep.* **5** (2015), 14880.

[33] H.-C. Liu et al. "Frequency-dependent polarization-angle-phase-shift in the microwave-induced magnetoresistance oscillations". *J. Appl. Phys.* **117** (2015), 064306.

[34] X. Fu et al. "Effect of density on microwave-induced resistance oscillations in back-gated GaAs quantum wells". *Phys. Rev. B* **98** (2018), 121303.

[35] Q. Shi et al. "Fine structure of high-power microwave-induced resistance oscillations". *Phys. Rev. B* **95** (2017), 041403(R).

[36] A. Wirthmann et al. "Far-infrared-induced magnetoresistance oscillations in GaAs/Al_xGa_{1-x}As-based two-dimensional electron systems". *Phys. Rev. B* **76** (2007), 195315.

[37] Z. D. Kvon et al. "Terahertz radiation-induced magnetoresistance oscillations of a high-density and high-mobility two-dimensional electron gas". *JETP Lett.* **97** (2013), 41–44.

[38] A. Chepelianskii et al. "Photogalvanic current in artificial asymmetric nanostructures". *Eur. Phys. J. B* **56** (2007), 323.

[39] S. A. Mikhailov. "Theory of microwave-induced zero-resistance states in two-dimensional electron systems". *Phys. Rev. B* **83** (2011), 155303.

[40] A. C. Durst et al. "Radiation-Induced Magnetoresistance Oscillations in a 2D Electron Gas". *Phys. Rev. Lett.* **91** (2003), 086803.

[41] I. A. Dmitriev, A. D. Mirlin, and D. G. Polyakov. "Cyclotron-Resonance Harmonics in the ac Response of a 2D Electron Gas with Smooth Disorder". *Phys. Rev. Lett.* **91** (2003), 226802.

[42] I. Dmitriev et al. "Theory of the oscillatory photoconductivity of a two-dimensional electron system". *Physica E* **25** (2004), 205–211.

[43] M. A. Zudov. "Comment on "Theory of microwave-induced zero-resistance states in two-dimensional electron systems" and on "Microwave-induced zero-resistance states and second-harmonic generation in an ultraclean two-dimensional electron gas"". *Phys. Rev. B* **92** (2015), 047301.

[44] S. A. Mikhailov. "Reply to "Comment on 'Theory of microwave-induced zero-resistance states in two-dimensional electron systems' and on 'Microwave-induced zero-resistance states and second-harmonic generation in an ultraclean two-dimensional electron gas' "". *Phys. Rev. B* **92** (2015), 047302.

[45] S. A. Mikhailov. "Microwave-induced magnetotransport phenomena in two-dimensional electron systems: Importance of electrodynamic effects". *Phys. Rev. B* **70** (2004), 165311.

[46] I. A. Dmitriev et al. "Theory of microwave-induced oscillations in the magnetoconductivity of a two-dimensional electron gas". *Phys. Rev. B* **71** (2005), 115316.

[47] D. J. H. Davies. *The Physics of Low-dimensional Semiconductors: An Introduction*. Cambridge University Press, 1997.

[48] M. Abramowitz and I. A. Stegun, eds. *Handbook of Mathematical Functions*. Dover Publications Inc., 1965. 1046 pp.

[49] T. Ihn. *Semiconductor Nanostructures: Quantum States and Electronic Transport*. Oxford Univ. Press, 2010. 580 pp.

[50] E. L. Ivchenko. *Optical Spectroscopy of Semiconductor Nanostructures*. Harrow: Alpha Science Int., 2005.

[51] K. Seeger. *Semiconductor Physics*. Wien: Springer-Verlag, 1973.

[52] T. Numai. *Fundamentals of Semiconductor Lasers (Springer Series in Optical Sciences)*. Springer, 2004.

[53] K. Seeger. *Semiconductor Physics: An Introduction*. Springer, 2004.

[54] E. H. Putley. "Far Infra-Red Photoconductivity". *physica status solidi (b)* **6** (1964), 571–614.

[55] S. Ganichev and W. Prettl. *Intense Terahertz Excitation of Semiconductors*. Oxford University Press, 2005.

[56] N. G. Asmar et al. "Energy relaxation at THz frequencies in $Al_xGa_{1-x}As$ heterostructures". *Semicond. Sci. Technol.* **9** (1994), 828.

[57] I. Kotel'nikov et al. "Heating of two-dimensional electron gas and LO phonons in δ-doped GaAs by far-infrared radiation". *Solid State Commun.* **97** (1996), 827–832.

[58] S. Dietrich et al. "Quantum lifetime of two-dimensional electrons in a magnetic field". *Phys. Rev. B* **85** (2012), 115312.

[59] V. Ryzhii. "Photoconductivity Characteristics in Thin Films Subjected to Crossed Electric and Magnetic Fields". *Sov. Phys. Solid State* **11** (1970), 2078.

[60] M. Khodas and M. G. Vavilov. "Effect of microwave radiation on the nonlinear resistivity of a two-dimensional electron gas at large filling factors". *Phys. Rev. B* **78** (2008), 245319.

[61] I. A. Dmitriev, S. I. Dorozhkin, and A. D. Mirlin. "Theory of microwave-induced photocurrent and photovoltage magneto-oscillations in a spatially nonuniform two-dimensional electron gas". *Phys. Rev. B* **80** (2009), 125418.

[62] I. A. Dmitriev et al. "Mechanisms of the microwave photoconductivity in two-dimensional electron systems with mixed disorder". *Phys. Rev. B* **80** (2009), 165327.

[63] A. A. Bykov. "Microwave-induced magnetic field state with zero conductivity in GaAs/AlAs Corbino disks and hall bars". *JETP Letters* **87** (2008), 551–554.

[64] M. J. E. Golay. "Theoretical Consideration in Heat and Infra-Red Detection, with Particular Reference to the Pneumatic Detector". *Rev. Sci. Instrum.* **18** (1947), 347–356.

[65] G. Abstreiter et al. "Cyclotron resonance of electrons in surface space-charge layers on silicon". *Phys. Rev. B* **14** (1976), 2480–2493.

[66] T. Herrmann et al. "Analog of microwave-induced resistance oscillations induced in GaAs heterostructures by terahertz radiation". *Phys. Rev. B* **94** (2016), 081301(R).

[67] Q. Zhang et al. "Superradiant Decay of Cyclotron Resonance of Two-Dimensional Electron Gases". *Phys. Rev. Lett.* **113** (2014), 047601.

[68] M. G. Vavilov and I. L. Aleiner. "Magnetotransport in a two-dimensional electron gas at large filling factors". *Phys. Rev. B* **69** (2004), 035303.

[69] M. A. Zudov et al. "Multiphoton processes in microwave photoresistance of two-dimensional electron systems". *Phys. Rev. B* **73** (2006), 041303.

[70] S. I. Dorozhkin et al. "Microwave induced magnetoresistance oscillations at the subharmonics of the cyclotron resonance". *JETP Letters* **86** (2007), 543–547.

[71] I. V. Pechenezhskiĭ, S. I. Dorozhkin, and I. A. Dmitriev. "Fractional features in radiation-induced oscillations of the magnetoresistance of two-dimensional electron systems". *JETP Letters* **85** (2007), 86–91.

[72] S. Wiedmann et al. "High-order fractional microwave-induced resistance oscillations in two-dimensional systems". *Phys. Rev. B* **80** (2009), 035317.

[73] X. L. Lei and S. Y. Liu. "Multiple and virtual photon processes in radiation-induced magnetoresistance oscillations in two-dimensional electron systems". *Appl. Phys. Lett.* **88** (2006), 212109.

[74] I. A. Dmitriev, A. D. Mirlin, and D. G. Polyakov. "Theory of Fractional Microwave-Induced Resistance Oscillations". *Phys. Rev. Lett.* **99** (2007), 206805.

[75] V. F. Gantmakher and Y. B. Levinson. *Carrier Scattering in Metals and Semiconductors (Modern Problems in Condensed Matter Sciences) (English and Russian Edition)*. Elsevier Science Ltd, 1987.

[76] T. Ihn. *Electronic Quantum Transport in Mesoscopic Semiconductor Structures*. Springer, 2004. 270 pp.

[77] V Karpus. "Effect of electron-phonon interaction on the ionization of deep centers by a strong electric field". *JETP Lett.* **44** (1986), 430–433.

[78] Y. H. Xie et al. "Power loss by two-dimensional holes in coherently strained Ge0.2Si0.8/Si heterostructures: Evidence for weak screening". *Appl. Phys. Lett.* **49** (1986), 283–285.

[79] E. Beregulin et al. "Sov. Phys.-JETP 70, 1138 (1990)". *Sov. Phys.-JETP* **70** (1990), 1138.

[80] T. Herrmann et al. "Magnetoresistance oscillations induced by high-intensity terahertz radiation". *Phys. Rev. B* **96** (2017), 115449.

[81] M. Otteneder et al. "Sign-alternating photoconductivity and magnetoresistance oscillations induced by terahertz radiation in HgTe quantum wells". *Phys. Rev. B* **98** (2018), 245304.

Acknowledgments

An dieser Stelle möchte ich mich bei allen herzlichst bedanken, die diese Arbeit erst möglich gemacht haben

Der größte Dank gebührt Sergey Ganichev, der mir die großartige Möglichkeit gegeben hat in seiner Gruppe diese Arbeit durchzuführen. Danke, dass du nie den Glauben an mich verloren hast und mir immer deine Unterstützung hast angedeihen lassen.

Des Weiteren möchte ich mich sehr bei Vanya Dmitriev bedanken, der das theoretische Fundament dieser Doktorarbeit gelegt hat und jederzeit bereit war, auch meine naivsten Fragen zu beantworten. Insbesondere danke ich dir, dass du diese Arbeit gelesen und mit konstruktiver Kritik bereichert hast. Auch bei den Menschen, die die Proben für diese Arbeit zur Verfügung gestellt, und diese oft speziell für diese Arbeit und natürlich immer unter großem Zeitdruck hergestellt haben. Besonders zu erwähnen sind hier Andreas Bayer, Martin Oltscher und Thomas Kuczmik. Dank gilt auch Vasily Bel'kov und Dmitriy Kozlov, die viele Stunden im Labor und am Diskussionstisch mit mir verbracht und so einen erheblichen Anteil an dieser Arbeit haben. Dies gilt natürlich auch und besonders für meine drei Masterstudenten Bruno, Martin und Leo. Es hat Spaß gemacht mit Euch zusammen zu arbeiten und ich bin froh einen Teil des Weges mit jedem von Euch gegangen zu sein. Initiiert wurde diese Arbeit von Dmitry Kvon, unter dessen Anleitung ich die ersten TIRO in unserem Labor gemessen habe. Vielen Dank dafür!

An meine Kollegen Helene, Kathrin und Philipp gerichtet kann ich nur sagen: Danke für die tollen Jahre die wir zusammen durch dick und dünn gegangen sind. Als Team sind wir unschlagbar! Dir, Helene möchte ich besonders danken, dass du diese Arbeit gelesen und mir so bei der Vermeidung vieler Fehler geholfen hast. Auch meinen anderen Kollegen Sergey Danilov, Peter Olbrich, Tina Zoth, Christoph Drexler, Sebastian Stachel, Susi Candussio, Stefan Hubmann, Maximilian Otteneder, Hannelore Lanz, Christian Schneider und Toni Humbs danke ich sehr für die schöne Zeit die wir zusammen verbracht und die gute Arbeit die wir geleistet haben. Den zahllosen Master- und Bachelorstudenten

die während meiner Zeit hier Teil unseres Teams waren danke ich für all die schönen Erinnerungen die wir zusammen gesammelt haben.

Zu guter letzt danke ich meiner Familie. Danke Mama und Papa, dass Ihr mich zu dem gemacht habt, der ich bin und mich immer auf meinem Weg unterstützt habt. Danke Max, du bist der beste Bruder den man sich wünschen kann. Ich danke allen Freunden die die letzen Jahre an meiner Seite waren, insbesondere dir Andi, für die ausserordentliche Freundschaft die uns verbindet, du bist wie ein Bruder für mich. Ich danke auch meinen Schwiegereltern, die ihr Haus und ihr Leben mit uns teilen und es uns so erst ermöglichen Familie und Beruf unter einen Hut zu bringen. Zum Abschluß danke ich meinem wunderbaren Sohn Leo und meiner großartigen Frau Marina, die mich jede Stunde meines Lebens glücklich machen.